



# Bioorthogonal click chemistry-mediated conjugation of an anti-DR4 antibody to gold nanorods enhances its pro-apoptotic activity under near infra-red-light stimulation

Abdelmnim Radoua<sup>a,1</sup>, Mélanie Romain<sup>b,1</sup> , Elisa Chazeau<sup>c</sup>, Nadège Marthouret<sup>d</sup> , Fabien Picaud<sup>d</sup>, Guillaume Herlem<sup>d</sup> , Christine Goze<sup>c</sup> , Nadine Millot<sup>b</sup>, Olivier Micheau<sup>a,\*</sup> 

<sup>a</sup> Université Bourgogne Europe, Inserm, CTM, DesCarTes, 21078 Dijon, France

<sup>b</sup> Université Bourgogne Europe, CNRS, Laboratoire Interdisciplinaire Carnot de Bourgogne ICB UMR 6303, 21000 Dijon, France

<sup>c</sup> Université Bourgogne Europe, CNRS, ICMUB UMR 6302, 21000 Dijon, France

<sup>d</sup> Université Marie et Louis Pasteur, UFR-ST, Laboratoire SINERGIES (UR 4662), Besançon 25030, France

## ARTICLE INFO

### Keywords:

Gold nanorods  
Pro-apoptotic receptor activators  
Strain promoted azide-alkyne cycloaddition  
NIR activation  
Anti-tumor therapy

## ABSTRACT

Pro-apoptotic receptor activators (PARAs), including second-generation agonist antibodies and ligands targeting the TNF receptor superfamily such as TRAIL (TNF-Related Apoptosis-Inducing Ligand), represent a promising class of cancer therapeutics. Enhancing their apoptotic efficacy through multivalency or controlled thermal stimulation has been previously demonstrated. In this study, we report the design and optimization of gold nanorod (GNR)-based nanoconjugates for targeted PARA delivery under near-infrared (NIR)-induced mild hyperthermia. Three conjugation strategies—EDC/NHS coupling, Schiff base formation, and strain-promoted azide-alkyne cycloaddition (SPAAC)—were systematically evaluated. Surface functionalization of GNRs with  $-\text{COOH}$ ,  $-\text{NH}_2$ , and  $-\text{DBCO}$  groups was confirmed via UV-vis spectroscopy, surface-enhanced Raman spectroscopy (SERS), X-ray photoelectron spectroscopy (XPS), zeta potential analysis, and transmission electron microscopy (TEM). Bioactivity assays indicated that SPAAC-mediated click chemistry enabled superior retention of PARA functionality compared to conventional methods. Notably, GNRs conjugated with an anti-DR4 antibody selectively triggered apoptosis in cancer cells upon NIR exposure. These results demonstrate that SPAAC-mediated functionalization enables precise, bioactive nanocarriers for enhanced cancer cell apoptosis under photothermal control.

## 1. Statement of significance

This work presents a robust, bio-orthogonal conjugation strategy relying on click chemistry to immobilize pro-apoptotic antibodies on gold nanorods without loss of bioactivity.

The resulting nanoplatfrom enables targeted cancer cell killing under near-infrared-induced mild hyperthermia, with potential for real-time imaging.

This approach advances the design of multifunctional, antibody-functionalized nanomaterials for precision cancer therapy and diagnostics.

## 2. Introduction

Despite significant advances in radiotherapy, chemotherapy, immunotherapy and surgery, cancer remains a worldwide public health issue [1]. Thermal ablation or photothermal therapy (PTT) has emerged as a promising complementary strategy, offering localized tumor targeting while minimizing invasiveness. The core principle of PTT involves the design and application of photo-absorbing agents that efficiently convert light energy into heat. By converting light energy into heat through photo-absorbing agents, PTT can locally increase the temperature in a controlled manner, leading to tumor cell damage via apoptosis and coagulative necrosis [2]. Utilizing near-infrared (NIR) wavelengths, typically between 800 and 1200 nm, PTT enhances the

\* Corresponding author.

E-mail address: [omicheau@ube.fr](mailto:omicheau@ube.fr) (O. Micheau).

<sup>1</sup> Equal contribution.

efficacy of chemotherapeutic and immunotherapeutic agents within the “biological window”, where tissues exhibit minimal light absorption, thereby allowing deeper penetration and more effective treatment [3]. Despite its potential, the clinical application of PTT faces challenges related to limited tumor selectivity and, in some cases, insufficient efficacy. [4]. These limitations have prompted the exploration of improved photothermal agents and combination strategies. To address these limitations, the rational design of nanostructured photothermal agents has emerged as a critical research focus. Gold nanorods (GNRs), in particular, offer tunable localized surface plasmon resonance (LSPR) properties through precise control of their aspect ratio, enabling efficient absorption in the NIR region [5–9]. These plasmonic features allow for localized heating at tumor sites using relatively low laser intensities, thereby enhancing therapeutic outcomes while minimizing damage to surrounding tissues [5,6]. However, while GNRs are effective photothermal converters, their translation into targeted therapeutic platforms requires robust surface functionalization strategies that allow stable conjugation of bioactive molecules, such as therapeutic antibodies, without compromising particle stability or therapeutic efficacy [10–13].

Combining PTT with immunotherapy offers novel therapeutic opportunities. One such approach involves the use of pro-apoptotic receptor activators (PARAs), such as TRAIL (TNF-related apoptosis-inducing ligand), which selectively induce apoptosis in cancer cells by binding to death receptors DR4 and DR5 [14,15]. The latter can also trigger apoptosis upon binding of agonist antibodies targeting either DR4 or DR5. TRAIL belongs to the TNF superfamily, and more specifically, to the subgroup of ligands displaying proapoptotic activities [16,17], which also includes Fas ligand (FasL) [18], among these, only TRAIL and its derivatives appear to hold potential for cancer therapy due to their preferential targeting of cancer cells [19–22].

The therapeutic potential of PARAs is most of the time significantly enhanced when conjugated onto nanoscale materials, improving their valency and tumor-targeting capability [23–29]. Likewise, coupling TRAIL to maghemite nanoparticles (MNPs) not only increases ligand valency, thereby improving TRAIL-mediated receptor oligomerization and its pro-apoptotic potential, but also enables the remote-controlled induction of mild-hyperthermia, which further enhances TRAIL-induced apoptosis [24]. Consistent with an earlier study demonstrating that a mild-hyperthermia can significantly increase TRAIL-induced cell death [30], application of a laser or a magnetic field to locally increase the temperature using these MNPs proved sufficient to enhance tumor cell killing [24].

However, the design of effective strategies for the functionalization of antibodies or ligands onto nanoparticles poses significant challenges. Specifically, the choice of conjugation chemistry is critical, as it can profoundly impact the orientation and, consequently, the bioactivity of the immobilized therapeutic protein. Likewise, while covalent conjugation of TRAIL can be achieved either through its N-terminal or C-terminal end [31], functionalizing antibodies can sometimes compromise both their binding affinity and therapeutic activity [32–34]. Henceforth, non-covalent attachment strategies often suffer from instability and premature dissociation in biological environments [35], conventional covalent techniques, such as EDC/NHS chemistry [36], which target primary amines (e.g., lysines), typically result in random antibody orientation, potentially masking the antigen-binding site and reducing efficacy [37,38]. Strategies aiming for oriented conjugation, such as oxidizing Fc-region glycans to create aldehydes for Schiff base formation with amine-functionalized nanoparticles, can improve targeting specificity but risk damaging the antibody or ligand during the oxidation process, potentially diminishing bioactivity [39]. Seeking to overcome these limitations, bioorthogonal methods like strain-promoted azide-alkyne cycloaddition (SPAAC) click chemistry have emerged. This catalyst-free approach offers high selectivity and efficiency under physiological conditions, providing a powerful tool for site-specific conjugation while minimizing disruption to protein structure and function [40–43].

In this study, we aimed to develop a hybrid nanoparticle system that combines the tumor-targeting capabilities of an immunotherapy with the localized therapeutic effect of photothermal therapy. Our objective was to engineer GNR-based nanovectors functionalized with pro-apoptotic agents to selectively induce cancer cell death [14,44,45]. The choice of targeting DR4 was driven by the knowledge that while TRAIL binds both DR4 and DR5, DR5 activation can also trigger non-apoptotic, potentially pro-metastatic signaling pathways [44,46].

Gold nanorods were synthesized using a seed-mediated growth method [9,47,48], with secondary growth steps to precisely tune their LSPR to match the 808 nm laser used for PTT. Three conjugation strategies were then compared for attaching TRAIL, FasL, or anti-DR4 antibodies to the GNRs: EDC/NHS coupling, oriented Schiff base formation, and SPAAC click chemistry. Among these, the Schiff base method significantly impaired the target-binding properties and pro-apoptotic activity of the ligands. In contrast, both EDC/NHS coupling and SPAAC preserved apoptotic function, but only SPAAC conjugation maintained full antibody bioactivity. This allowed for a synergistic effect between NIR-mediated heating and DR4-mediated apoptosis, highlighting the promise of SPAAC-based nanovectors in advancing targeted combinatorial cancer therapy.

### 3. Materials and methods

#### 3.1. Materials

Tetrachloroauric acid trihydrate ( $\text{HAuCl}_4 \cdot 3\text{H}_2\text{O}$ , 99.99 %), N-hydroxysuccinimide (NHS,  $\text{C}_4\text{H}_5\text{NO}_3$ ,  $\geq 99$  %), HRP-conjugated rabbit anti-human IgG Fc secondary antibody (catalog #31423), and Slide-A-Lyzer dialysis cassettes with a molecular weight cut-off (MWCO) of 7000 Da (catalog #66710) were sourced from Thermo Fisher Scientific. Anti-His tag antibody (catalog #MCA1396) and Poly-Prep® chromatography columns (catalog #7311550) were obtained from Bio-Rad. Protein G Sepharose 4 Fast Flow resin (catalog #17061801) was purchased from Cytiva. Peroxidase AffiniPure™ goat anti-mouse IgG (H + L) (catalog #115-035-003) was acquired from Jackson ImmunoResearch Laboratories. Cyanin5-DBCO (catalog #FP-AWHFX0) was procured from Interchim. Potassium bromide (KBr) was supplied by Prolab. Sodium acetate ( $\geq 99.0$  %), cetyltrimethylammonium bromide (CTAB,  $\text{C}_{16}\text{H}_{42}\text{NBr}$ ,  $\geq 99.0$  %), sodium borohydride ( $\text{NaBH}_4$ ,  $\geq 96.0$  %), silver nitrate ( $\text{AgNO}_3$ ,  $\geq 99.0$  %), L-ascorbic acid ( $\text{C}_6\text{H}_8\text{O}_6$ ,  $\geq 99.0$  %), 1-ethyl-3-(3-dimethylaminopropyl)carbodiimide (EDC,  $\text{C}_8\text{H}_{17}\text{N}_3$ ,  $\geq 97.0$  %), DBCO-NH<sub>2</sub> ( $\text{C}_{18}\text{H}_{16}\text{N}_2\text{O}$ ), acetic acid ( $\text{CH}_3\text{CO}_2\text{H}$ ,  $\geq 99.7$  %) and dimethyl sulfoxide (DMSO,  $\text{C}_2\text{H}_6\text{OS}$ ,  $\geq 99.7$  %) were obtained from Sigma-Aldrich. HS-PEG(10 k)-COOH and HS-PEG(10 k)-NH<sub>2</sub> were acquired from Iris Biotech. All chemical reactions were conducted using analytical-grade solvents from Carlo Erba under ambient conditions. Anhydrous solvents were either used as received from Carlo Erba or dried with MB-SPS-800 (MBraun) or PureSolv-MD-5 (Inert) systems. Unless otherwise noted, all reagents from Thermo Fisher Scientific, Sigma-Aldrich, Iris Biotech, or BroadPharm were used without additional purification. Reaction progress was monitored using thin-layer chromatography (TLC) and reverse-phase HPLC-MS. TLC was performed with precoated silica gel 60F<sub>254</sub> plates (0.2 mm thickness, Merck). Silica gel column chromatography was conducted using 40–63  $\mu\text{m}$  particle size silica (230–400 mesh, 60 Å pore size; Sigma-Aldrich). Annexin V-FITC (catalog #BLE640945) and 7-AAD (catalog #BLE420404) were obtained from BioLegend Europe (Amsterdam, Netherlands). Dialysis membranes with 12–14 kDa MWCO (Spectrum Lab Spectra/Por) were obtained from Fisher, while 300 kDa MWCO dialysis tubing was acquired from Interchim (catalog #131450 T). All aqueous solutions were prepared using ultrapure water with resistivity exceeding 18.2 M $\Omega$ -cm.

### 3.2. GNRs synthesis and functionalization

GNRs were synthesized by seed-mediated growth method with secondary growth procedure. All glassware were pre-washed with aqua regia. Primary growth solution was prepared in 77 mL of 0.122 M CTAB solution heated at 30 °C. Then, 1 mL of 0.95 M KBr, 1 mL of 22.4 mM AgNO<sub>3</sub>, 20 mL of 4.8 mM HAuCl<sub>4</sub>·3H<sub>2</sub>O, and 1 mL of 0.11 M L-ascorbic acid were successively added to the CTAB solution under stirring. Seeds solution was prepared at 30 °C by a combination of 8 mL of 0.125 M CTAB solution, 1 mL of 0.10 M KBr solution, 1 mL of a 2.8 mM HAuCl<sub>4</sub>·3H<sub>2</sub>O solution, after what 0.6 mL of 10 mM NaBH<sub>4</sub> was injected under stirring, for 2 min before being left for 3 min. 136 µL of the seeds solution was injected in the primary growth solution and stirred vigorously for a few seconds before being left for an hour to let GNRs grow. GNRs size and shape was then homogenized by a secondary growth consisting of the addition of 5 mL of a 9.5 mM L-ascorbic acid solution at a 1.8 mL/h rate. Resulting suspension was finally centrifuged twice at 8000 G for 15 min and resuspended in 0.15 mM CTAB.

GNRs functionalization with HS-PEG10k-COOH and HS-PEG10k-NH<sub>2</sub> followed ligand exchange mechanism. A PEG solution was injected to GNRs suspension with an Au:S = 1:0.24 M ratio. The mixture was sonicated for one hour before being stirred for one hour. Resulting suspension was washed twice by centrifugation at 5000 G for 10 min and resuspended in water. Final suspensions were called GNR-COOH and GNR-NH<sub>2</sub> respectively.

### 3.3. Coupling strategies

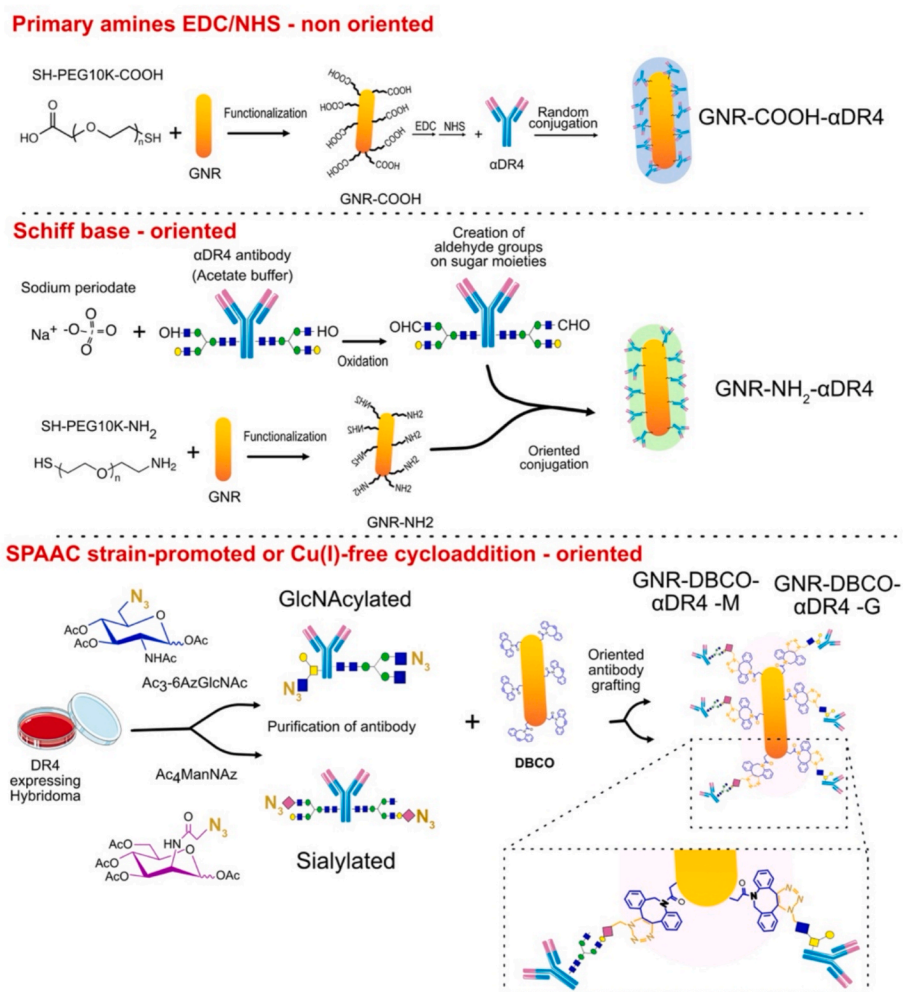
The three different GNRs to antibody coupling strategies are schematized in [scheme 1](#).

#### Amide coupling of protein to GNR-PEG10K-COOH using EDC/NHS

1 mL of GNR-COOH were activated by successive injection of EDC 3 mM and NHS 6 mM under stirring with a final molar ratio Au:EDC:NHS of 1:0.045:0.09. Antibody (Ab) solution in PBS buffer was then injected in a Au:Ab mass ratio equals to 1:0.5. Mixture was stirred 2 h at room temperature (RT) and next stirred overnight at 4 °C. Resulting suspension was finally dialyzed twice using 300 kDa MWCO dialysis tube in 1 Liter of PBS1X.

#### Sugar moieties oxidation and conjugation of proteins to GNR-PEG10K-NH<sub>2</sub>

Antibodies and Fc-fusion proteins were dialyzed in 50 mM acetate buffer (pH 4.2) and diluted at a concentration of 1 mg/mL in 10 mM NaIO<sub>4</sub> (sodium periodate; freshly prepared at 200 mM in acetate buffer). The mixture was then incubated at 4 °C for 2 h. Samples were then dialyzed in PBS1X using Slide-A-Lyzer dialysis cassettes 7 kDa MWCO (ref#66370, ThermoFisher) for 8 h at 4 °C and diluted to 0.1 mg/mL of protein. Antibody function was analyzed *via* flow cytometry and oxidation of sugar moieties was verified using 4-amino-3-hydrazino-5-mercapto-1,2,4-triazole (sc-209923, Santa Cruz Biotechnology) which generates a purple dye and an absorbance at 550 nm (not shown).



**Scheme 1.** Illustration of the different coupling strategies compared in this study. Top: Random coupling using EDC/NHS chemistry targeting primary amines on the antibody. Middle: Oriented grafting *via* glycan oxidation followed by Schiff base formation and reduction. Bottom: Site-specific conjugation using bioorthogonal click chemistry enabled by a metabolic labeling approach.

Oxidized antibodies and Fc-fusion proteins were mixed (overnight, 4 °C, gentle agitation on a rotor) with GNR-PEG10K-NH<sub>2</sub> at a weight ratio of 1:0.5 (GNR:Protein). To generate stable covalent bond between antibody or Fc-Fusion proteins and GNR-NH<sub>2</sub>, sodium borohydride (NaBH<sub>4</sub>, Sigma) was added (4 μmole for each 10 μg of antibody) and incubated for no more than 45 min (at 4 °C with gentle agitation on a rotator) to reduce Schiff base intermediates and then dialyzed twice using 300 kDa MWCO dialysis tube (ref#MPE30025, Merck) in 1 Liter of PBS1X.

#### SPAAC click chemistry oriented conjugation

10 mL of GNR-COOH were activated by successive injection of EDC 3 mM and NHS 6 mM under stirring with a final molar ratio Au:EDC:NHS of 1:0.045:0.09. A solution of 5 mM DBCO-NH<sub>2</sub> in DMSO was added with a molar ratio Au:DBCO of 1:0.045 (final 0.8 % (v/v) DMSO). The mixture was stirred overnight at 20 °C and next washed by dialysis (12–14 kDa cut-off) in water. 1 mL of the newly synthesized GNR-PEG10K-DBCO was incubated with azide-containing proteins (antibodies or Fc-fusion protein produced in presence of Ac<sub>4</sub>ManNAz or Ac<sub>3</sub>6AzGlcNAc, leading for the antibody to GNR-DBCO-α-DR4-M and -G, respectively) at a weight ratio of 1:0.5 (GNR:protein) for 4 h at 20 °C. To avoid aggregation of GNRs, free DBCO groups on GNR were quenched using AzaBODIPY-azide at 20 °C for 2 h. The suspension was finally dialyzed twice (300 kDa cut-off) in fresh 1 Liter PBS buffer to remove excess proteins and AzaBODIPY-N<sub>3</sub>.

### 3.4. Synthesis of Wazaby-N<sub>3</sub>

**Compound 1** (refer to Fig. S1) was synthesized following a previously described method [49].

**Synthesis of Compound 2** (Fig. S2): Compound 1 (74 mg, 108 μmol, 1 eq) was dissolved in 15 mL of acetonitrile (CH<sub>3</sub>CN). Sodium bicarbonate (NaHCO<sub>3</sub>, 45 mg, 541 μmol, 5 eq) and propanesultone (11.5 μL, 130 μmol, 1.2 eq) were added sequentially. The resulting mixture was refluxed overnight. Upon completion, the reaction mixture was filtered to remove the excess of base and was concentrated under reduced pressure. The crude product was purified by semi-preparative high-performance liquid chromatography (HPLC) and lyophilized, yielding Compound 2 as a dark green solid (45 mg, 52 % yield).

**NMR and MS characterization of Compound 2:** <sup>1</sup>H NMR (500 MHz, MeOD, 298 K) δ (ppm): 8.41 (d, *J* = 9.0 Hz, 4H), 8.11 (d, *J* = 9.0 Hz, 4H), 7.52–7.41 (m, 6H), 7.32 (s, 2H), 7.25 (d, *J* = 9.0 Hz, 4H), 3.96 (s, 2H), 3.95 (s, 6H), 3.70 (s, 2H), 3.40–3.34 (m, 2H), 2.95 (t, *J* = 6.7 Hz, 2H), 2.82 (s, 6H), 2.68 (s, 6H), 2.21–2.11 (m, 2H).

<sup>13</sup>C NMR (126 MHz, MeOD, 298 K) δ (ppm): 163.7, 159.4, 144.5, 144.4, 143.9, 134.3, 133.9, 130.7, 130.7, 130.0, 130.0, 126.1, 125.7, 121.5, 121.3, 115.8, 115.4, 93.5, 87.3, 64.2, 63.9, 56.8, 56.6, 56.2, 51.3, 50.9, 44.3, 30.0, 20.2. <sup>11</sup>B NMR (160 MHz, MeOD) δ (ppm): –12.75 (br s).

**RP-HPLC-MS:** Calculated for C<sub>47</sub>H<sub>48</sub>BN<sub>5</sub>O<sub>5</sub>S<sup>+</sup> [M]<sup>+</sup>: 805.35 Da; observed: 806.5 Da.

**Analytical HPLC:** Retention time (tR) = 4.05 min; purity: 98 %.

**Synthesis of Wazaby-N<sub>3</sub>** (Fig. S3): Compound 2 (16 mg, 20 μmol, 1 eq) was dissolved in 5 mL of anhydrous CH<sub>3</sub>CN. Sodium bicarbonate (8.3 mg, 99 μmol, 5 eq) and a solution of bromo-PEG<sub>4</sub>-azide (32 mg, 99 μmol, 5 eq) in 200 μL of dry CH<sub>3</sub>CN, 100 mg/mL) were added. The reaction mixture was refluxed for 48 h. The inorganic base was removed by filtration, and the solvent was then evaporated under reduced pressure. The crude material was purified by semi-preparative HPLC and lyophilized to afford Wazaby-N<sub>3</sub> as a dark green powder (12 mg, 52 % yield).

**NMR and MS characterization of Wazaby-N<sub>3</sub>:** <sup>1</sup>H NMR (500 MHz, MeOD, 298 K) δ (ppm): 8.45 (d, *J* = 9.0 Hz, 4H), 8.13 (d, *J* = 9.0 Hz, 4H), 7.53–7.43 (m, 6H), 7.41 (s, 2H), 7.27 (d, *J* = 9.0 Hz, 4H), 4.17 (s, 2H),

3.96 (s, 6H), 3.88 (s, 2H), 3.83–3.79 (m, 2H), 3.57–3.51 (m, 2H), 3.50–3.42 (m, 16H), 3.23 (t, *J* = 6.6 Hz, 2H), 3.02 (s, 6H), 2.88 (t, *J* = 6.6 Hz, 2H), 2.77 (s, 6H), 2.15–2.11 (m, 2H).

<sup>13</sup>C NMR (126 MHz, MeOD, 298 K) δ (ppm): 163.9, 159.0, 144.3, 143.9, 134.2, 133.6, 130.8, 130.5, 130.0, 125.5, 121.3, 115.6, 93.5, 87.3, 71.7, 71.6, 71.6, 71.4, 71.3, 71.1, 65.9, 63.8, 56.6, 52.6, 51.9, 51.1, 30.9, 20.2. <sup>11</sup>B NMR (160 MHz, MeOD) δ (ppm): –12.10 (br s).

**RP-HPLC-MS:** Calculated for C<sub>57</sub>H<sub>68</sub>BN<sub>8</sub>O<sub>9</sub>S<sup>+</sup> [M]<sup>+</sup>: 1051.5 Da; observed: 1051.7 Da.

**Analytical HPLC:** Retention time (tR) = 4.13 min; purity: 98 %.

### 3.5. Grafting efficiency quantification

Anti-His tag, anti-Mouse IgG and anti-Human IgG antibodies were used for western-blot semiquantitative estimation of grafted ligands or antibodies in GNRs suspensions after dialysis. The determined quantity was then normalized in each case to the sample volume and GNRs concentration (determined via NTA) in order to express the grafting efficiency in ng of protein/μg of GNRs.

### 3.6. Cell culture and antibody or ligand production

Hybridoma producing anti-TfR1 (OKT-9 clone) or anti-DR4 antibodies used for grafting were obtained from LG Standards (ref# ATCC-CRL-8021) or Covalab [45], respectively and amplified in DMEM High Glucose (Dutscher, ref# L0104-500) containing 20 % of heat inactivated FBS. The wild-type TNBC (triple negative breast carcinoma) cell line, MDA-MB-231 (ATCC ref# HTB-26) and the embryonic kidney cell line HEK293T (ATCC ref# CRL-3216) were cultured in DMEM High Glucose supplemented with 10 % FBS (Dutscher, Brumath, France) at 37 °C in the presence of 5 % CO<sub>2</sub> and saturated humidity. The DR4 and DR5 double knock-out cell line (MDA-MB-231) was generated using TALENs (Transcription activator-like effector nuclease) as described elsewhere [44] and cultured similarly to the wild-type cell line. Fc-FasL and Fc-TRAIL were produced via transfection of corresponding expression vectors using PEI (Dutscher, ref# X0515-500) reagent on HEK293T cells. Opti-MEM Reduced Serum Medium, supplemented with GlutaMAX (ThermoFisher, ref# 51985026), containing when indicated Ac<sub>4</sub>ManNAz (10 μM; Cliniscience, ref# HY-118297) or Ac<sub>3</sub>6AzGlcNAc (10 μM; Click Chemistry Tools ref# 1258), was used for producing the antibodies or the Fc-fused ligands. The proteins of interest, contained in the supernatants, were collected after 5 days of production and purified using a column containing Protein-G Sepharose 4FF beads using and acidic elution buffer (100 mM glycine, pH2.7), followed by a neutralization step using Tris (1 M Tris, pH9).

His-tagged wild-type TRAIL or TRAIL-Mut3 [49] were produced using BL21 (DE3) pLysS Escherichia coli as described in Radoua et al. 2023 [50].

Depending on the application, the buffer was exchanged for the purified antibodies or ligands by dialysis against either PBS or Acetate buffer, using Slide-A-lyzer® Dialysis cassettes (7000 MWCO).

For cytotoxicity studies, 2 × 10<sup>4</sup> or 1 × 10<sup>6</sup> cells were seeded into 96 or 6 well plates, respectively, and incubated overnight. For cell death kinetics, 96 well plates were used with Incucyte®S3 at a 10X magnification. Annexin V-FITC was added to the wells at a final dilution of 1/500th. The cells were treated with the GNRs or soluble ligands as described in the result section. For fluorescence and brightfield images-based quantification, the following parameters were used in the Incucyte® software: For precise quantification of cytotoxicity, cells were recovered (detached and adherents) and 0.75 ng of 7AAD was added per sample, 10 min before analysis by flow cytometry.

Brightfield	Segmentation adjustment 0.6	Area ( $\mu\text{m}^2$ ) filter <100		
Green Fluorescence	Segmentation type Surface-Fit	Threshold (GCU) 1.5	Edge split ON Edge sensitivity: 0	Area ( $\mu\text{m}^2$ ) filter <30

### 3.7. GNR-mediated PTT in-vitro

Cell treated with  $1 \times 10^{10}$  particles/mL of grafted GNR were stimulated using 918 mW NIR laser operating at  $\sim 180 \text{ mW/cm}^2$  and 808 nm (ref# LRD-0808 Collimated Diode Laser System, Laserglow) combined with an optic fiber (ref# MAF3L1, Thorlabs) to ensure that NIR laser rays are delivered accurately to target area (96 well plates for  $1.5 \times 10^4$  adherent cells or 0.2 mL containing  $1 \times 10^6$  cells treated in suspension). Temperature detection is carried out using an infrared camera (detection wavelength is 8 to 14  $\mu\text{m}$ ), the Xi410 model from Optris.

### 3.8. Characterizations

**Transmission Electron Microscopy (TEM):** Gold nanorods (GNRs) morphology and size were characterized using a Hitachi HT7800 TEM operating at 100 kV. Sample preparation involved drop-casting a diluted GNR suspension onto carbon-coated copper grids followed by solvent evaporation.

**Nanoparticle Tracking Analysis (NTA):** Concentration and hydrodynamic size distribution of GNRs (expressed in particles per mL) were analyzed using a NanoSight NS300 system (Malvern Instruments, UK). Instrumental settings included a sCMOS camera, a 488 nm blue laser, camera level 12, and detection threshold 5. Prior to acquisition, the suspension was equilibrated for 20 s post-injection. Each measurement consisted of three 60 s video recordings at 25 °C, with data averaged across the replicates for final analysis.

**UV-Vis Spectroscopy (LSPR Characterization):** Localized surface plasmon resonance (LSPR) of GNRs was evaluated by UV-Vis absorbance measurements using a Thermo Multiskan GO microplate reader (Thermo Fisher Scientific). Aliquots of 200  $\mu\text{L}$  were transferred into 96-well plates. Spectra were collected from 400 to 1000 nm, with deionized water serving as the baseline reference.

**Surface-Enhanced Raman Spectroscopy (SERS):** SERS measurements were performed on dried GNR suspensions using a Renishaw InVia microspectrometer. A 785 nm diode laser and a  $50 \times$  microscope objective were employed for excitation and signal collection.

**X-ray Photoelectron Spectroscopy (XPS):** Surface elemental composition was assessed using a PHI 5000 VersaProbe system with a monochromatic Al K $\alpha$  X-ray source (energy = 1486.7 eV). A 200  $\mu\text{m}$  beam spot, 12 kV accelerating voltage, and 200 W power were applied. Samples were prepared by sequential deposition of GNR suspension droplets on a silicon wafer. Spectral fitting and data processing were conducted using the CasaXPS software suite.

**Zeta Potential Measurements:** The surface charge of GNRs in suspension was measured using a Malvern Zetasizer Nano ZS (Malvern Instruments, UK), operated with DTS Nano v7.11 software. Measurements were conducted using an absorption coefficient of 3.320 and refractive index of 0.200, corresponding to gold nanoparticles.

**Nuclear Magnetic Resonance (NMR) Spectroscopy:**  $^1\text{H}$ ,  $^{13}\text{C}$ ,  $^{11}\text{B}$ , and  $^{19}\text{F}$  NMR spectra were recorded at 298 K using a Bruker Avance Neo 500 MHz spectrometer equipped with a 5 mm BBOF iProbe. Chemical shifts ( $\delta$ ) are reported in parts per million (ppm) relative to internal standards: Tetramethylsilane TMS ( $^1\text{H}$ ,  $^{13}\text{C}$ ),  $\text{BF}_3 \cdot \text{Et}_2\text{O}$  ( $^{11}\text{B}$ ), and  $\text{CFCl}_3$  ( $^{19}\text{F}$ ). Calibration was performed using residual solvent signals, and for other nuclei, external reference-based zero calibration was used. Measurements were performed at the "Plateforme d'Analyse Chimique et de

Synthèse Moléculaire de l'Université de Bourgogne" (PACSMUB).

**RP-HPLC-MS Analysis:** Reverse-phase HPLC-MS analyses were conducted on a ThermoFisher Vanquish system equipped with a UV-Vis diode array detector and an ISQ-EM single quadrupole mass spectrometer. The system included a temperature-controlled autosampler (20 °C) and column oven (25 °C). Separations were performed on a Phenomenex Kinetex C18 column (2.6  $\mu\text{m}$ ,  $2.1 \times 50 \text{ mm}$ ) using a binary gradient of acetonitrile with 0.1 % formic acid (solvent B) and 0.1 % aqueous formic acid (solvent A, pH 2.1). The elution gradient ranged from 5 % to 100 % B over 5 min, followed by isocratic elution at 100 % B for either 3 or 5 min (for hydrophobic compounds), at a flow rate of 0.5 mL/min. UV detection was performed at 214, 254, 280, and 650 nm, with full-spectrum collection from 220–700 nm. Mass spectra were recorded in both positive and negative electrospray ionization (ESI) modes, using full scan acquisition (100–1000  $m/z$ ), centroid mode, 1 s scan time. Instrumental parameters included: source CID voltage = 20 V; vaporizer temperature = 282 °C; ion transfer tube = 300 °C; positive mode voltage = +3 kV; negative mode voltage = -2 kV; sheath gas pressure = 49.9 psig (3.4 bar); auxiliary gas = 5.7 psig (0.35 bar); sweep gas = 0.5 psig (0.035 bar).

**Semi-Preparative HPLC Purification:** Purification procedures were carried out on a Shimadzu semi-preparative HPLC system composed of two LC-20AT pumps, a SPD-20A UV/Vis detector, SIL-10AP autosampler, FRC-10A fraction collector, and CBM-20A controller. Chromatographic separation was achieved using a SiliCycle C18 column (10  $\mu\text{m}$ ,  $10 \times 250 \text{ mm}$ ) with a binary mobile phase of water (0.1 % formic acid) and acetonitrile. The flow rate was maintained at 20 mL/min. The elution gradient was programmed as follows:

Time (min)	% H <sub>2</sub> O (0.1 % FA)	% ACN
0	90	10
2	90	10
5	80	20
65	20	80

UV detection was conducted at 220, 260, 600, and 700 nm.

**Photophysical Characterization:** UV-Vis absorption spectra were recorded using a SAFAS FLX-Xenius spectrophotometer. Absorption maxima ( $\lambda_{\text{max}}$ , nm) and molar extinction coefficients ( $\epsilon$ ,  $\text{M}^{-1} \cdot \text{cm}^{-1}$ ) were determined. Fluorescence emission spectra were measured under steady-state conditions using the same instrument. Spectra were corrected for instrument response. Measurements were performed in quartz cuvettes (1.5 mL, 1 cm path length) with sample concentrations adjusted to yield absorbances of 0.3–1.0 for UV and 0.035–0.1 at the excitation wavelength for quantum yield ( $\Phi$ ) determinations.

Relative quantum yields were calculated by comparison with a standard aza-BODIPY derivative ( $\Phi = 0.36$  in  $\text{CHCl}_3$ ,  $\lambda_{\text{exc}} = 670 \text{ nm}$ ) [52]. All measurements were conducted in DMSO (spectroscopic grade  $\geq 99.9 \%$ , Sigma-Aldrich) and PBS at 298 K. The quantum yield was computed using the following equation:

$$\Phi_x = \Phi_{\text{ref}} \left( \frac{\text{Grad}_x}{\text{Grad}_{\text{ref}}} \right) \left( \frac{\eta_{\text{ref}}^2}{\eta_x^2} \right)$$

Where  $\Phi$  is the fluorescence quantum yield, Grad is the slope of the integrated fluorescence intensity vs. absorbance plot at the excitation wavelength, and  $\eta$  is the solvent refractive index (DMSO: 1.477;  $\text{CHCl}_3$ : 1.446; PBS: 1.337).

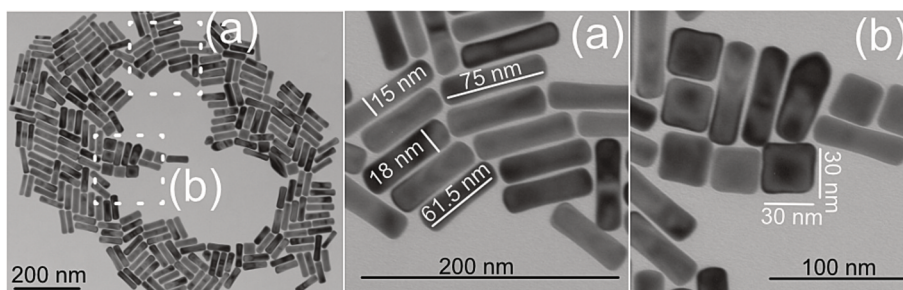


**Fig. 1.** TEM images of synthesized gold nanorods (GNRs). (a) and (b) show magnified views. The dimensions of the GNRs (width and length) are indicated in nm.

### 3.9. Statistical analysis

Differences between selected groups were compared to non-parametric one-way analysis of variance (ANOVA) with Tukey's multiple comparison test. All statistical analyses were performed using Prism version 10.2.3 software (GraphPad Software, San Diego, CA.). P values  $<0.05$ ,  $**<0.01$ ,  $***p < 0.001$  and  $****p < 0.0001$  were considered significant.

## 4. Results and discussion

### 4.1. Synthesis of the GNRs

Gold-nanorods were characterized by TEM as shown in Fig. 1. The average size of the synthesized GNRs (Fig. 1) was  $75.6 \pm 6.3$  nm length and  $18.1 \pm 2.6$  nm in width. Predominantly, monodisperse GNRs were obtained (Fig. 1-a), though other shapes such as spheres, cubes, and bipyramids were also observed, albeit in smaller quantities (Fig. 1-b).

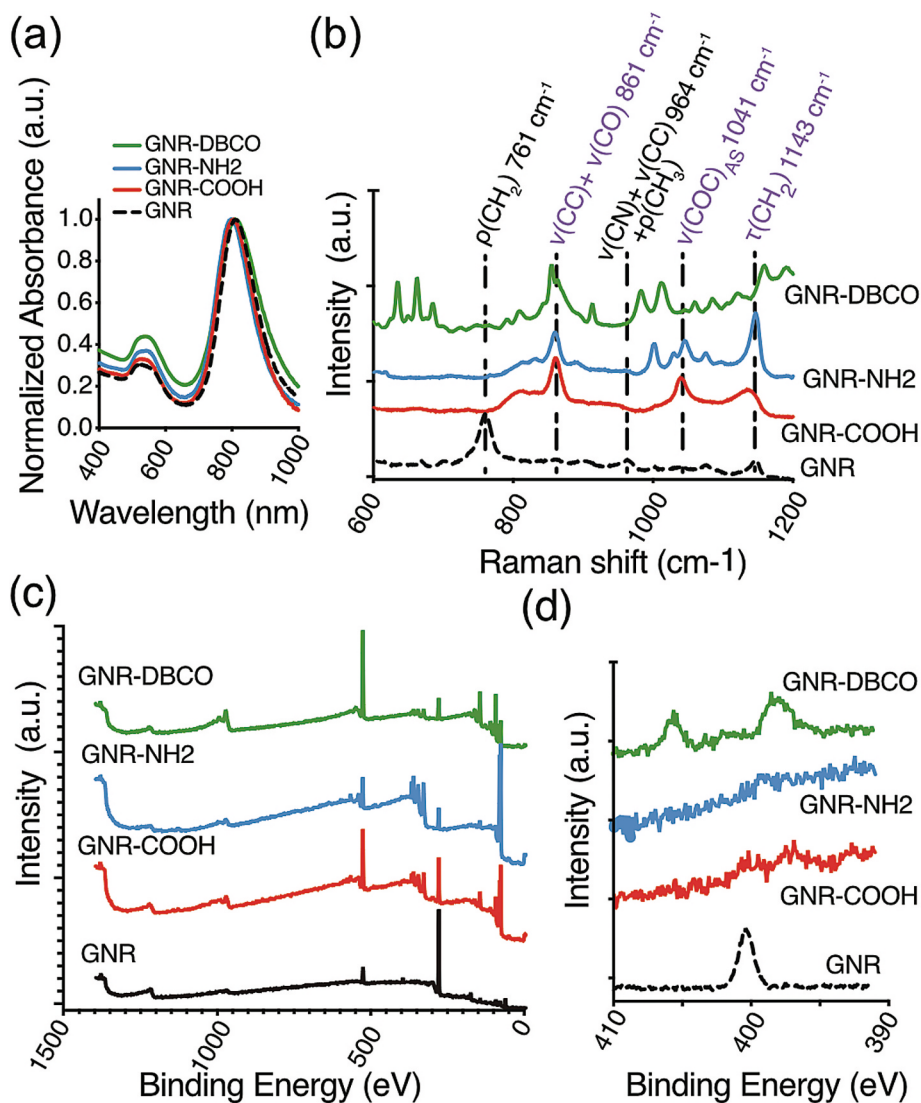


**Fig. 2.** (a) UV-visible spectra, (b) Raman spectra, (c) XPS spectra, and (d) high-resolution N1s XPS spectra of the GNRs, either unmodified or functionalized with various PEG derivatives, including DBCO.

The resulting suspension exhibited a transverse localized surface plasmon resonance (LSPR) band at 524 nm and a very intense longitudinal LSPR band at 812 nm (Fig. 2-a). This is favorable for photothermal applications, especially with laser stimulation typically used at 808 nm, where temperatures up to 80 °C were achieved at varying concentrations (not shown).

After functionalization with either carboxylated or aminated PEG, a shift in the LSPR profile was observed (Fig. 2-a), attributable to the change in refractive index of the surrounding PEG molecules around the GNRs [51]. To confirm the presence of grafted PEGs, Raman spectroscopy, zeta potential measurements, and XPS measurements were performed. Surface-enhanced Raman spectroscopy (SERS) spectra present the differences between CTAB-capped GNRs and PEGylated GNRs (Fig. 2-b).

Characteristic CTAB bands are visible in the GNR spectra at 761  $\text{cm}^{-1}$  and 964  $\text{cm}^{-1}$  corresponding to  $\text{CH}_2$  deformation and C-N and C-C stretching with  $\text{CH}_3$  deformation, respectively [52]. These peaks are absent in the PEGylated GNRs spectra. For GNRs-COOH and GNRs-NH<sub>2</sub>, intense bands appear at 861  $\text{cm}^{-1}$  and 1143  $\text{cm}^{-1}$ , attributed to skeleton vibration of PEG and twisting vibration of  $\text{CH}_2$  [53]. Additionally, a band at 1041  $\text{cm}^{-1}$ , present only in the PEGylated GNRs spectra, corresponds to antisymmetric stretching and confirms the presence of PEG molecules on the GNRs [54]. X-ray photoelectron spectroscopy (XPS) spectra (Fig. 2-c) for the N1s region show a weak peak for GNRs, but only background noise for PEGylated GNRs. High-resolution spectra of Au 4f for all sample are presented in (Fig. 2-d).

The atomic concentrations inferred from the XPS analysis are detailed in Table 1 and show the relative amounts of O1s, C1s, and N1s.

Nitrogen is present in the initial CTAB-capped GNRs, where CTAB was used in excess. However, after PEGylation, the samples do not seem to contain any nitrogen. This is even true for aminated PEG, for which nitrogen was not detected due to its presence within the high molecular mass polymer and the relatively low sensitivity of XPS, which is around 0.1 %. The absence of nitrogen in PEGylated GNRs suggests the removal of cytotoxic CTAB, making these GNRs suitable for further biological studies. The increased amount of oxygen around 30 and 40 % in the functionalized GNRs, indicates efficient PEG grafting. Finally, the difference between the suspensions was evaluated by their zeta potential measurement. At a pH of 6, CTAB-capped GNRs had a zeta potential (ZP) value of +40.6 mV, which shifted to -24.3 mV for GNRs-COOH and 0.3 mV for GNRs-NH<sub>2</sub> (Fig. S4). This shift reflects the replacement of the positively charged quaternary ammonium headgroup of CTAB with the respective PEGylated functional groups. The negative ZP for GNRs-COOH confirms the presence of deprotonated carboxyl groups ( $-\text{COO}^-$ ), while the near-neutral ZP (0.3 mV) for GNRs-NH<sub>2</sub> at pH 6 is consistent with the primary amine groups being only partially protonated near their effective surface pKa (Fig. S4). Importantly, despite the near-neutral ZP of GNRs-NH<sub>2</sub> offering limited electrostatic repulsion, the presence of the long (10 k) PEG chains provides significant steric hindrance. This steric stabilization mechanism is expected to contribute to colloidal stability, and indeed, the functionalized GNR suspensions appeared initially stable against immediate aggregation following preparation and during characterization.

**Table 1**

Atomic concentrations of selected elements determined by XPS analysis for GNRs, PEGylated GNRs, CTAB, and the various PEG derivatives.

Sample	C1s (%)	O1s (%)	N1s (%)
GNRs	92.8	3.9	3.3
GNRs-COOH	70.1	29.2	0
GNRs-NH <sub>2</sub>	61.4	38.0	0
CTAB	94.4	0.7	4.4
HS-PEG(10 k)-COOH	66.8	33.1	0
HS-PEG(10 k)-NH <sub>2</sub>	66.7	33.2	0

#### 4.2. EDC/NHS-mediated functionalization of PARAs and biological assessment

EDC/NHS-mediated functionalization of PARAs onto nanoparticles has been reported to maintain or even sometimes enhance their biological antitumoral activity [24,31]. For instance, we have demonstrated that TRAIL could be functionalized to maghemite nanoparticles through carboxylic or amino groups without altering its pro-apoptotic activity [31]. Similarly, conjugating TRAIL to 100 nm magnetite nanoclusters via EDC/NHS chemistry not only modestly enhanced TRAIL's apoptotic activity but also enhances TRAIL's anti-tumoral potential, at equivalent concentrations, when combined with a laser or an electromagnetic field to induce mild hyperthermia [24].

To avoid the unwanted pro-motile signaling properties of DR5 [44,55], we first use an anti-DR4 antibody ( $\alpha$ -DR4), along with two other PARAs, the soluble TRAIL (TRAIL-8R or mut3 [49]) or Fc-Fas ligand [56], as a proof of concept. These were conjugated to COOH-functionalized GNRs using EDC/NHS. Our objective was to compare the pro-apoptotic activity of these functionalized nanoparticles to their soluble counterparts. Following functionalization and dialysis, GNRs were analyzed using NTA. As shown in Fig. 3, the mean size of the GNRs ranged from 74 to 106 nm, with the majority measuring between 72 and 76 nm  $\pm$  4 nm.

The pro-apoptotic potential of GNR-COOH grafted with PARAs was assessed against the triple negative breast cancer cell line MDA-MB-231 or its isogenic cell line derivative, engineered to lack both DR4 and DR5 expression (DKO) [44]. Notably, PEG-functionalized GNR-COOH exhibited no toxicity towards MDA-MB-231 cells, regardless of concentration (Fig. 4a and 4c). This result confirms the absence of CTAB in the final preparation, the compound used to cap GNRs during their synthesis, which is highly toxic for cells, consistent with the XPS findings.

As expected, GNR-COOH-TRAIL-8R retained comparable pro-apoptotic activity as soluble TRAIL-8R, inducing apoptosis in WT MDA-MB-231 cells in a dose-dependent manner (Fig. 4-a). However, as expected, it failed, even at the highest tested concentration, to induce apoptosis in the TRAIL-receptor deficient MDA-MB-231 DKO cells (Fig. 4-b). Consistently too, functionalization of soluble Fas ligand (Fc-Fas L), another PARA, also enabled the preservation of Fas ligand's pro-apoptotic potential, as assessed in both the WT MDA-MB-231 and MDA-MB-231 DKO cells (Fig. 4-c), consistent with the fact that both isogenic cell lines express Fas, the cognate Fas ligand receptor (not shown). Functionalization of the anti-DR4 using the EDC/NHS, although less efficient in inducing apoptosis [45], as compared to TRAIL-8R or Fc-Fas ligand (Fig. 4), also retained, albeit to a lower extent, the antibody's pharmacological properties (Fig. 4-e and 4-f). The direct effect of these functionalized GNRs is visually represented in Fig. S5, where cell morphology and apoptosis (green staining) are shown in the presence of GNR-COOH-Fc-FasL, GNR-COOH-TRAIL-8R, GNR-COOH- $\alpha$ -DR4 or void GNR (GNR-COOH), in both the parental and TRAIL-deficient DKO cells.

#### 4.3. Schiff base strategy for oriented functionalization of PARAs and biological assessment

Given that TRAIL-induced apoptosis relies on the full engagement of the agonist receptors [57,58], we aimed to optimize the orientation of our agonists pro-apoptotic receptor activators (PARAs) [15], to maximize the activation of TRAIL or Fas agonist receptors. We first explored the Schiff base strategy, which involves the oxidation of polysaccharides contained in the heavy chain of most immunoglobulins, to orientate the conjugation of the antibodies onto GNRs. Because TRAIL does not harbor glycosylation site, contrary to FasL which harbors both putative N- and O-glycosylation sites [16], we opted to functionalize a recombinant version of TRAIL fused to the human constant immunoglobulin chain (Fc-TRAIL), similar to Fc-FasL. This strategy yielded GNRs with a mean size ranging from 95 to 127 nm  $\pm$  7 nm (Fig. 5), approximately 20 nm

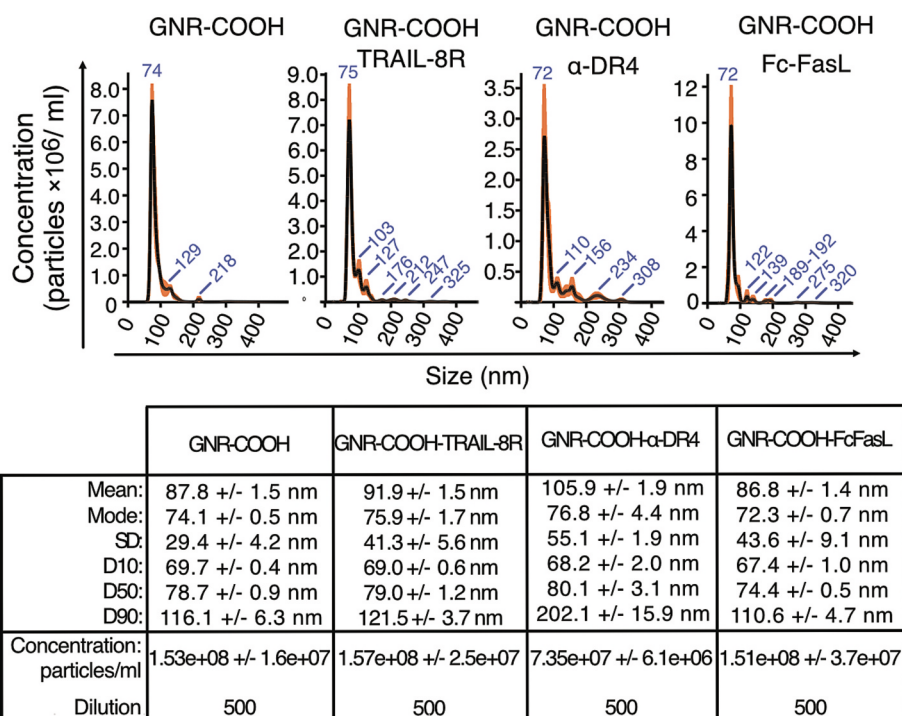


Fig. 3. NTA analysis of GNR-COOH conjugates functionalized via EDC/NHS coupling with TRAIL-8R, Fc-FasL or an anti-DR4 monoclonal antibody.

larger than GNR-COOH (74 to 106 nm).

Covalent binding through the Schiff base strategy, contrary to EDC/NHS, however, did not preserve the antitumoral activity of the tested PARAs. Likewise, none of the functionalized PARAs, including Fc-FasL, were able to induce apoptosis in MDA-MB-231 parental cells (Fig. 6a), despite the high sensitivity of these cells to Fas ligand (Fig. 4c and Fig. 6b). Likewise, Annexin-V staining, an early apoptosis marker, was detectable with Fc-FasL at concentrations as low as 160 pg/mL (Fig. 6-b).

The absence of enhanced functionality with the Schiff base strategy, compared to EDC/NHS (Fig. 4), is likely due to the oxidation step, which may have significantly altered the immunoreactivity of the ligands and/or antibodies. This hypothesis is supported by the finding that in addition to the loss of pro-apoptotic activity, as described above, oxidation of our antibody targeting DR4 drastically impaired its binding capabilities (Fig. 6-d). By contrast, oxidation of the anti-TfR1 antibody ( $\alpha$ -TfR1) did not affect its binding to MDA-MB-231 cells (Fig. 6-e), indicating that the loss of reactivity is not universal. However, since TfR1 does not trigger cell death, GNR- $\text{NH}_2$ - $\alpha$ -TfR1 remained non-toxic to MDA-MB-231 cells (Fig. 6-a). These findings suggest that the Schiff base functionalization approach is not suitable for the TNF superfamily ligands or antibodies tested in this study, due to the detrimental effects of oxidation on their immunoreactivity.

#### 4.4. SPAAC click chemistry strategy for oriented functionalization of PARAs and biological assessment

In order to avoid the loss of immunoreactivity due to the oxidation step, we next explored the strain-promoted alkyne-azide cycloaddition (SPAAC) click chemistry strategy to graft an anti-DR4 agonist antibody. For this approach, PEG-10K-DBCO GNRs were synthesized and characterized using XPS, UV-Visible spectroscopy, and Raman spectroscopy (Fig. 2). The addition of new bands in the SERS spectra indicates the presence of DBCO groups (Fig. 2-b), and a weak N1s peak was detected in the XPS analysis (Fig. 2-c). The DBCO-coupled GNRs were slightly smaller than GNR-COOH or GNR- $\text{NH}_2$ , with an average size of  $61.4 \pm 0.9$  nm as determined by NTA. This reduction in size may be due to the

hydrophobic nature of the DBCO groups causing a contraction in the molecular layer surrounding the GNRs.

Functionalization of the  $\alpha$ -DR4, as seen from two independent batches, yielded larger nanoparticles than those obtained with other functionalization techniques. The size of the GNR-DBCO particles ranged from 59 to over  $126 \text{ nm} \pm 20 \text{ nm}$  (Fig. S6). To enhance stability, prevent aggregation, and enable *in vivo* optical imaging, reactive sites on the GNRs were quenched with Wazaby-N3, an Aza-BODIPY (AzaB) derivative. Wazaby refers to a water-soluble AzaB. Aza-BODIPYs present numerous advantages compared to other fluorophores [59–61], including high chemical and photochemical stability, as well as excellent photophysical properties in the NIR-I region (700–900 nm). Their poor water solubility [61], however, makes their use for biological applications challenging. A strategy was therefore previously devised to improve their hydrophilicity, by substituting the fluorine atoms on the boron atom with propargylamine derivatives [62], resulting in the development of the so called Wazaby dyes. Using this method, compound 1 was easily obtained and was next desymmetrized to add on one side a water-solubilizing group (in this case, a sulfonate group) and on the other side a PEG moiety bearing an azide function (Fig. S1). A detailed characterization (HPLC chromatogram and NMR spectrum) of compound 2 and Wazaby-N3 is provided Figs. S2 and S3, respectively, as well as photophysical characterizations (Fig. S7 and Table S1).

Conjugation of Wazaby-N3 to the remaining DBCO sites of the nanoparticles efficiently prevented their aggregation (not shown). Additionally, this quenching step with Wazaby-N3 allowed for the semi-quantitative immunoblotting of the anti-DR4 antibody, as well as other PARAs, to approximate the amount of protein functionalized onto the GNRs. Specifically, GNRs samples loaded onto SDS-polyacrylamide gels (Fig. S8-a) after heat denaturation and reduction, as shown in Fig. S8-b, could be semi-quantified against known concentrations of soluble anti-DR4 antibody. The denaturation process appeared to break the covalent bonds linking the antibody to the GNR, thereby facilitating quantification (Fig. S8-b). However, without heating and reduction, a large proportion of the antibody remained attached to the GNRs, as evidenced by the presence of immunoreactivity in the stacking gel (Fig. S8-b).

Similarly, AzaB was visible in the SDS-PAGE, but unlike the



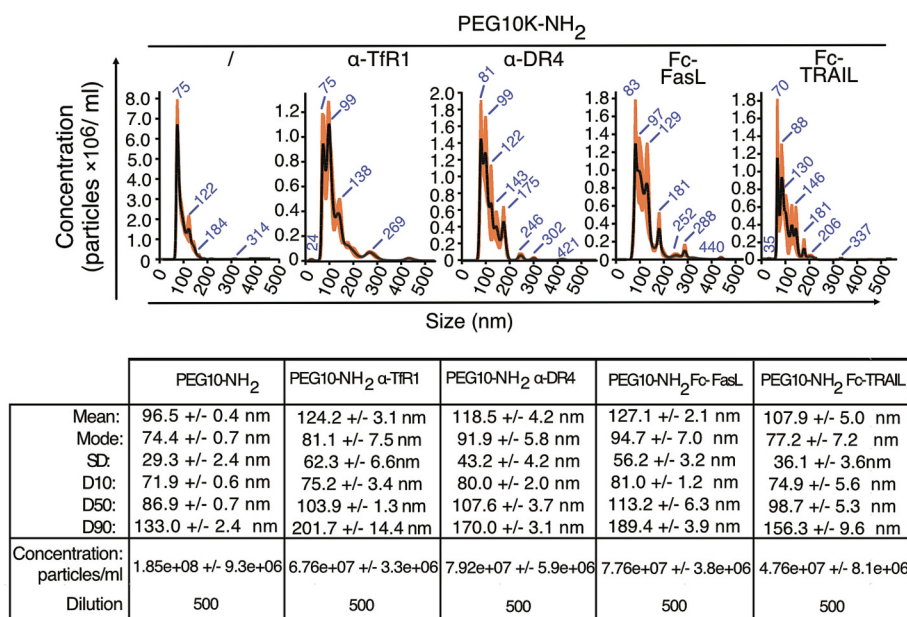


Fig. 5. NTA analysis of GNR-NH<sub>2</sub> (PEG10K-NH<sub>2</sub>) functionalized using the Schiff base strategy with Fc-TRAIL, Fc-FasL, anti-TfR1 or an anti-DR4 monoclonal antibodies.

treatment (Fig. 7), further highlighting the specificity of this formulation.

#### 4.5. Effects of DR4-functionalized gold nanorod-mediated photothermal therapy on cell viability and apoptosis in MDA-MB-231 cell lines

We then assessed whether the pro-apoptotic activity of the GNR-DBCO-AzaB (GNR-DA) conjugated with the anti-DR4 antibody (GNR-DA-α-DR4) could be enhanced by NIR photothermal therapy (PTT) in MDA-MB-231 cells as illustrated Fig. 8-a. First, we evaluated the hyperthermic properties of GNR-DAs under NIR, which resulted in a significant, time-dependent temperature increase in treated wells compared to untreated controls (Fig. 8-b). Infrared thermal imaging further confirmed this effect, revealing localized “hot spots” reaching approximately 43 °C within less than three minutes of NIR exposure, demonstrating the efficient photothermal conversion capability of the GNRs (Fig. 8-b).

The combination of (GNR-DA-α-DR4) and PTT led to a marked reduction in cell viability over time in MDA-MB-231 but not in DR4-deficient cells, as measured by real-time microscopy using the Incu-cyte S3 live microscope device (Fig. 8-c). To quantify more precisely the percentage of MDA-MB-231 cells undergoing apoptosis after NIR photothermal therapy, we modified the experimental settings (Fig. 8-c). Specifically, instead of stimulating cells in 96-well plates at 2x10<sup>4</sup> adherent cells per well, in 200 μL, as shown in Fig. 8-a, we stimulated cell in suspension (1x10<sup>6</sup> cells) in the same volume but this time in a 1.5 mL micro-Eppendorf tube. This adjustment was chosen in order to be able to maintain the laser’s focus and to compare the effects of PTT with mild hyperthermia, which was induced by incubating the cells in a water bath at 42 °C for 1 h (Fig. 8-d).

With the experimental setup illustrated in Fig. 8-d, we demonstrated that mild-hyperthermia, induced either by a short 1 h exposure of the cells at 42 °C or a 3 to 5 min time stimulation with a NIR laser (808 nm), consistently and significantly enhanced the pro-apoptotic activity of GNR-DA-α-DR4 in MDA-MB-231 cells (Fig. 8-e and -f). Flow cytometry dot plots revealed a pronounced increase in Annexin V-FITC and 7AAD staining in cells treated with GNR-DA-α-DR4, particularly when subjected to mild hyperthermia (Fig. 8-e). While treatment with either GNR-DA-α-DR4 alone or hyperthermia (42 °C incubation) resulted in 10 % to 18 % apoptosis in parental MDA-MB-231 cells, their combination

significantly increased cell death to 40 %. This effect was further amplified to 50 % with the addition of NIR exposure (Fig. 8-f). In contrast, MDA-MB-231 DKO cells, which lack DR4, exhibited 6 % cell death in untreated conditions, 8 % with GNR-DA-α-DR4 alone, and 18 % with hyperthermia alone. Notably, combining GNR-DA-α-DR4 with hyperthermia in these cells resulted in no additional increase, maintaining apoptosis at 18 % (Fig. 8-f). As expected, the combined PTT and GNR-DA-α-DR4 treatment in MDA-MB-231 DKO cells did not significantly alter the apoptotic rates compared to mild hyperthermia alone, yielding 18 % to 19 % cell death with either an incubation at 42 °C or a stimulation with NIR (Fig. 8-f).

Altogether, our findings demonstrate that conjugating an anti-DR4 antibody to gold nanorods can efficiently enhance its pro-apoptotic activity under PTT in DR4-expressing MDA-MB-231 wt cells. The study underscores the potential of this innovative approach, where the synergy between PTT and apoptosis induction significantly enhances cell death. Utilizing GNR-antibody conjugates combined with NIR represents a promising strategy, extending beyond anti-DR4 antibodies, to trigger apoptosis in cancer cells, leveraging the localized heating effect to amplify pro-apoptotic activity.

#### 4.6. Discussion

Pro-apoptotic receptor activators (PARAs), particularly TRAIL receptor agonists, have been explored as promising oncology targets [63–65], despite setbacks in clinical trials due to the discontinuation of several formulations and their combinations with conventional chemotherapies [64–66]. For example, the recombinant TRAIL dulanermin has reached a phase III clinical trial to evaluate its efficacy combined with an alkylating agent (*cis*-platinum) and a vinca alkaloid (vinorelbine), that interferes with microtubule assembly, for treating patients suffering from non-small cell lung cancer (NSCLC) [67]. The study demonstrated that the combination of dulanermin with chemotherapy significantly improved both progression-free survival and objective response rates. However, the trial also revealed a synergistic toxic profile in the cohort of 342 patients with advanced NSCLC (stage IIB and IV), attributed primarily to conventional chemotherapeutic drugs rather than TRAIL. These findings confirm the safety of TRAIL administered to patients but underscore the critical need for optimized TRAIL formulations.

The first generation of PARAs were either produced as soluble

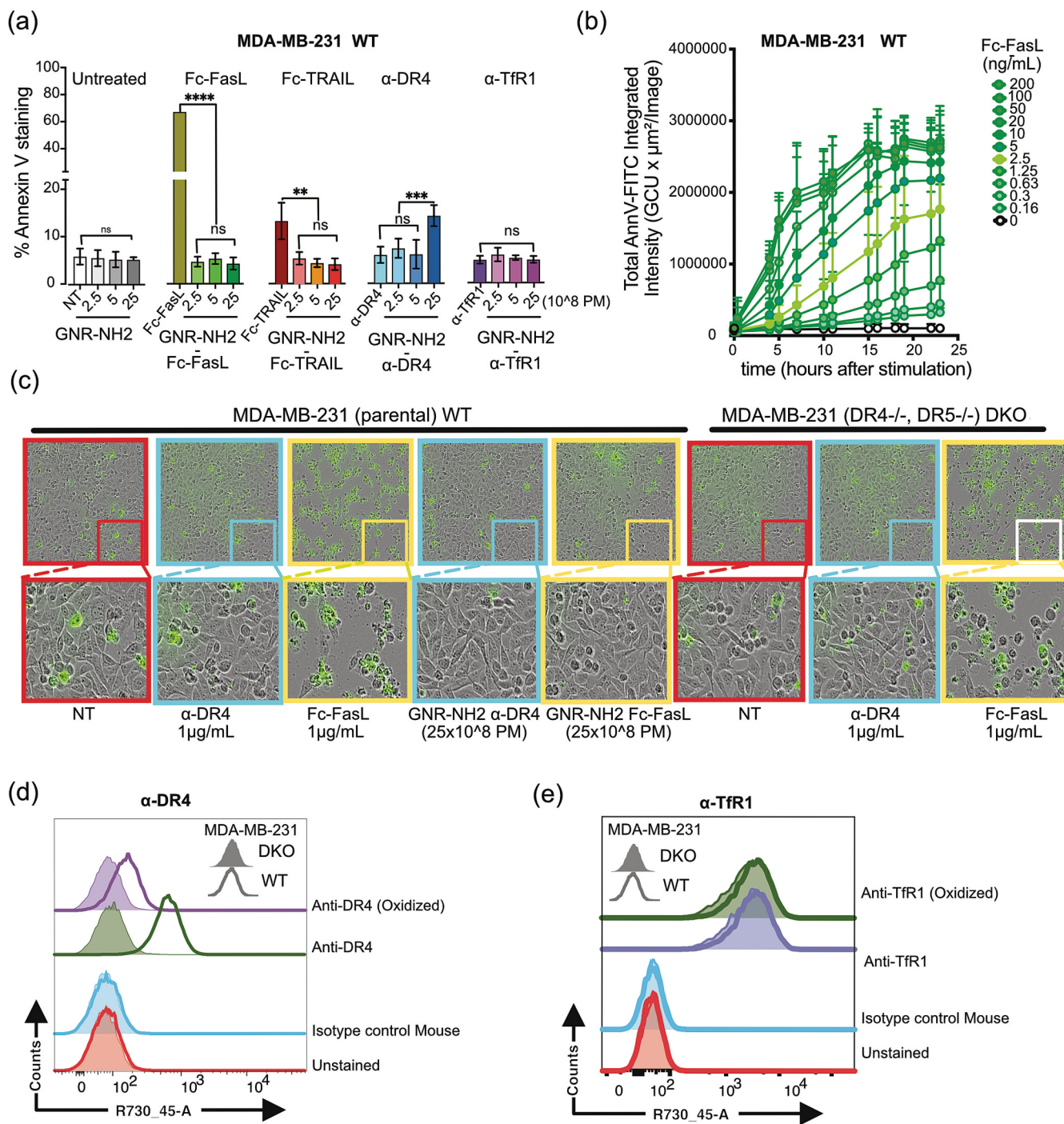


**Fig. 6.** Assessment of the pro-apoptotic function of TNF ligands and anti-DR4 antibodies grafted onto GNRs using oxidation and Schiff base reduction. (a) Parental MDA-MB-231 cells (WT) were treated for 24 h with TRAIL (Fc-TRAIL and anti-DR4) or Fas (Fc-FasL) receptor agonists, either grafted onto GNRs or in their free form, as described in the materials and methods. Apoptosis was quantified using Annexin V staining and flow cytometry. Nanoparticle concentrations for stimulation were 2.5, 5, or 25  $\times$  10<sup>8</sup> particles/mL (PM). Fas and TRAIL receptor agonists were used at a concentration of 1000 ng/mL. TfR1 was included as a control. (b) Dose-dependent apoptotic response of WT MDA-MB-231 cells to increasing concentrations of Fc-FasL, quantified using Annexin V staining and S3 Incucyte® live-cell imaging. Data are expressed as arbitrary units of fluorescence intensity. (c) Representative fluorescence and phase-contrast images of Annexin V-stained MDA-MB-231 cells treated as in (b), with selected magnified views at 16 h. Green, rounded, and detached cells indicate Annexin V+ cells undergoing apoptosis. Images of MDA-MB-231 DKO cells, which lack both DR4 and DR5, after stimulation with Fc-FasL and anti-DR4 antibody are also shown. (d) and (e) Flow cytometric analysis of WT and DKO MDA-MB-231 cells stained with anti-DR4 or anti-TfR1 antibodies, either oxidized or unmodified. Unstained and isotype control antibodies are included for reference. Empty histograms correspond to MDA-MB-231 DKO cells, while filled histograms show parental (WT) cells. Statistical significance, based on three independent experiments, is indicated as follows \*\*p < 0.01, \*\*\*p < 0.001, \*\*\*\*p < 0.0001. (For interpretation of the references to colour in this figure legend, the reader is referred to the web version of this article.)

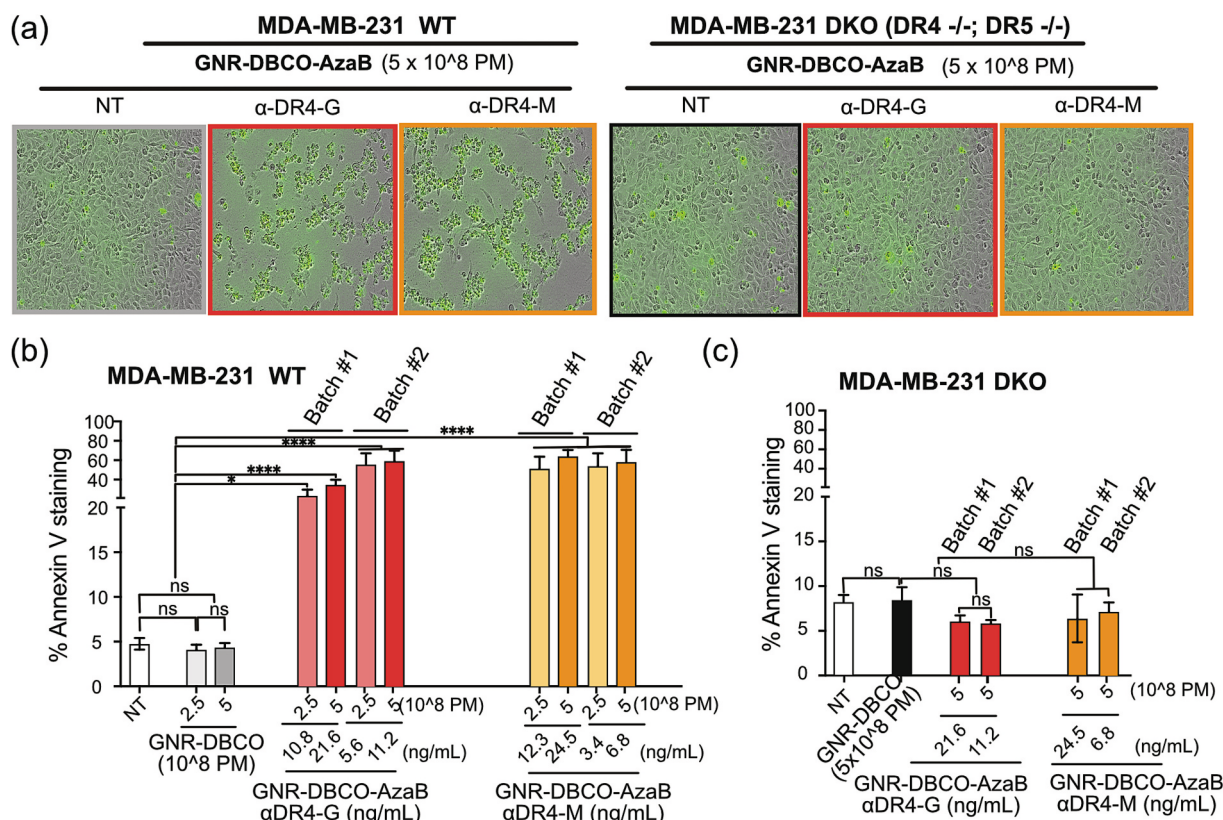


**Fig. 7.** Evaluation of the pro-apoptotic function of anti-DR4 antibody grafted onto GNRs using SPAAC click chemistry. (a) Parental (WT) or TRAIL-Deficient DKO MDA-MB-231 cells were stimulated with GNRs functionalized with anti-DR4 antibody ( $\alpha$ -DR4) using either AC3-6AzGlcNAc (G) or AC4ManNAz (M), respectively and merged annexin V fluorescent staining / brightfield pictures of treated cells were collected 8 and 16 h after stimulation, using the S3 Incucyte®. (b) Parental (WT) or (c) TRAIL-receptor-Deficient DKO MDA-MB-231 cells were stimulated as described above with increasing amounts of GNRs, and apoptosis was quantified by flow cytometry. Statistical significance from three independent experiments is indicated as: \* $p < 0.05$ , \*\*\*\* $p < 0.0001$ .

trimeric form (TRAIL) or divalent agonist antibodies. These formulations are not optimized to trigger apoptosis in cancer cells, their relatively low valency does not allow proper receptor oligomerization and caspase-8 activation [68]. As demonstrated in our study (Fig. 7) and corroborated by previous research studies [25,31,69–72], increasing the valency of anti-TRAIL-receptor agonists or TRAIL itself increases their pro-apoptotic potential. This principle is now well-admitted worldwide, prompting the development of second-generation PARAs [14,23], with higher valency to improve their efficacy and clinical translation. Approaches to increasing TRAIL valency include engineering a single TRAIL chain fused to the heavy chain of human immunoglobulins, such as Eftozanermin alfa (Eftoza), currently in clinical trials by ABBVIE [69] or TRAIL receptor agonist antibody isotype class switching to IgMs [73]. Additionally, various nanoparticle-based strategies have been explored to enhance TRAIL's pro-apoptotic potential [70,71,74–76].

To our knowledge, our study is the first to report a nanoformulation that combines the site specific orientation of anti-DR4 antibodies with gold nanorods (GNRs) using bioorthogonal click chemistry, thereby maximizing receptor engagement and therapeutic selectivity. Previous work involving DR5 antibody conjugation to GNRs typically relied on EDC/NHS chemistry [77,78], which leads to random, often inefficient antibody orientation. Our study provides, thus the demonstration that conjugation of an agonistic anti-DR4 antibody onto GNRs via bio-orthogonal DBCO-mediated click chemistry significantly enhances its pro-apoptotic potential. This effect is further amplified when combined with PTT, leveraging the photothermal properties of GNRs. Compared to conventional EDC/NHS conjugation, bioorthogonal click chemistry enabled oriented functionalization of the DR4 antibody, providing stronger pro-apoptotic activity. In contrast, Schiff base-oriented functionalization, abolished DR4 antibody's

immunoreactivity due to the oxidation step, completely inhibiting its pro-apoptotic potential. Furthermore, while EDC/NHS, in our hands, with the exception of TRAIL (Fig. 4-a), did not increase PARAs pro-apoptotic activity, as evidenced with Fc-FasL or the anti-DR4 antibody (Figs. 4 and 7), the click chemistry approach significantly increased apoptosis induction. These findings were supported by immunochemical estimations of PARA conjugation yields and comparable cell death percentages across equivalent PARA concentrations. Thus, only the oriented click chemistry strategy successfully enhanced the pro-apoptotic activity of the DR4 agonist antibody.

A key achievement of this work is the substantial and reproducible antibody loading attained on the GNRs via our SPAAC methodology. Our semi-quantitative analysis definitively shows typical grafting densities of 8 to 15 ng of anti-DR4 antibody per  $\mu$ g of GNRs (Supplementary Fig. S8-e), corresponding approximately 11 to 21 antibody molecules per individual GNR. Notably, this experimentally determined range closely aligns with theoretical predictions based on nanoparticle surface area and steric constraints. Although precisely calculating the absolute maximum antibody capacity is inherently complex at the nanoscale level, a rational design-based estimate serves as a useful benchmark for evaluating functionalization efficiency. The complexity arises from: (i) deviations between the geometric surface area ( $\sim 4303 \text{ nm}^2$  from TEM-based models) and the chemically available surface due to atomic-scale surface features and potential impurities; (ii) the conformational behavior of the PEG(10 k)-DBCO layer, which may adopt "mushroom" or "brush" structures that modulate surface accessibility [79,80]; (iii) the effective footprint of the conjugated antibody (an IgG is  $\sim 14.5 \text{ nm} \times 8.5 \text{ nm}$ ), which, despite site-specific conjugation aiming for an "end-on" orientation (estimated footprint  $\approx 50\text{--}70 \text{ nm}^2$ ), can exhibit some orientational flexibility and requires significant spacing [81–83]; (iv)

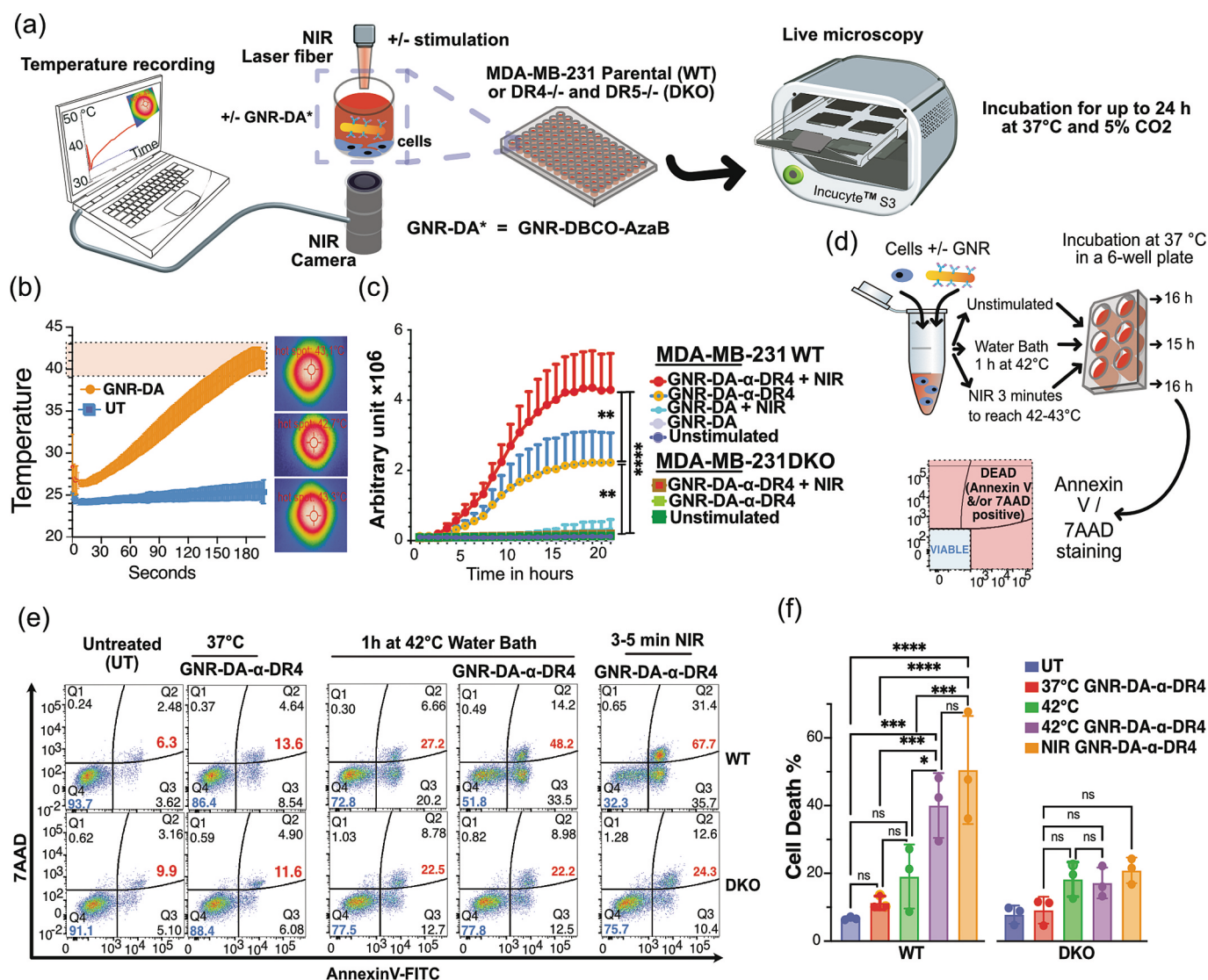


**Fig. 8. Enhanced Pro-Apoptotic Potential through the Combination of GNR-DBCO-AzaB- $\alpha$ -DR4 and NIR Stimulation** (a) Schematic illustration of the experimental setup used to record temperature changes and cell death overtime in a 96-well plate, where cells are exposed to Gold Nanorods (GNRs) under near-infrared (NIR) radiation. Apoptosis was tracked using the live microscope Incucyte S3 system. (b) Average temperature increase over time in cells exposed to NIR stimulation. Time-dependent temperature changes in cells treated with GNRs (+GNR-DA) and without (–GNR-DA) across eight independent experiments are shown as indicated in orange and blue lines, respectively. The right panel shows three examples of infrared thermal images highlighting “hot spots” at different temperatures (43.1 °C, 42.7 °C, 43.3 °C) during NIR exposure in GNR-treated cells. (c) Time-lapse analysis of apoptosis in wild-type (WT) MDA-MB-231 cells (upper panel) and double knockout (DKO) cells (lower panel) treated with GNR- $\alpha$ -DR4 combined with photothermal therapy (PTT), GNR- $\alpha$ -DR4 alone, GNR-PTT, GNR alone, and unstimulated controls. Apoptosis was assessed using Annexin V staining using the Incucyte S3 system, with results presented in arbitrary units over a 20 h period. (d) Schematic illustration of the second experimental design with which PTT was applied to cells in suspension in a 200  $\mu$ L micro-Eppendorf tube as indicated. (e) Representative flow cytometry dot plots showing Annexin V-FITC and 7-AAD staining in WT and DKO cells, either untreated or treated with GNR- $\alpha$ -DR4, with or without PTT as described in (d). (f) Quantification of cell death in WT and DKO cells, either untreated or treated with GNR- $\alpha$ -DR4 at 37 °C or following PTT as indicated in panel (d). Statistical significance from three independent experiments is indicated as: \* $p < 0.05$ , \*\* $p < 0.01$ , \*\*\* $p < 0.001$ , \*\*\*\* $p < 0.0001$ . (For interpretation of the references to colour in this figure legend, the reader is referred to the web version of this article.)

substantial steric hindrance from already bound, bulky antibodies impeding the approach of subsequent antibodies to nearby reactive sites; (v) the practical impossibility of achieving 100 % DBCO functionalization on all PEG linkers due to their dynamic nature and ensuring all DBCO groups are optimally exposed; and (vi) the intrinsic efficiency limitations of the DBCO-azide click reaction on a crowded and heterogeneous nanoparticle surface[84].

Accounting for these design constraints, we estimated a geometric upper limit of  $\sim 71$  antibodies per GNR, and applied a conservative packing efficiency factor of  $\sim 0.2$  to reflect steric and functionalization limitations. This yields a theoretical grafting density of  $\sim 14$  antibodies per GNR, or  $\sim 12.2$  ng of antibody per  $\mu$ g of GNRs—remarkably

consistent with our experimental findings. The strong agreement between predicted and measured values, combined with high inter-batch reproducibility (Fig. S7-e), highlights the efficiency and robustness of our functionalization platform. These results reinforce the suitability of the SPAAC method for achieving controlled and predictable biointerface design in antibody-functionalized nanomaterials.

Gold nanorods have emerged as a highly versatile platform for photothermal therapy (PTT), owing to their strong near-infrared (NIR) absorption and tunable plasmonic properties. The design of such GNR-based theranostics has seen significant progress. Pioneering work by Huang et al. demonstrated the dual functionality of anti-EGFR antibody-conjugated GNRs in targeted cancer cell imaging and selective

photothermal ablation [10]. Through the application of surface plasmon resonance, these GNRs enabled efficient destruction of malignant cells at half the laser energy required for nonmalignant counterparts. Advances in conjugation strategies, particularly strain-promoted azide-alkyne cycloaddition (SPAAC) using DBCO chemistry, have significantly improved antibody orientation and preserved bioactivity [85], underscoring the importance of sophisticated material surface engineering. Combinatorial platforms, such as cisplatin-polypeptide-wrapped GNRs, have demonstrated synergistic effects by integrating chemotherapy with PTT, effectively suppressing tumor growth in triple-negative breast cancer models [86]. These strategies capitalize on the high photothermal conversion efficiency of GNRs under optimized laser parameters, which enables localized hyperthermia (~41–42 °C) [87]. Beyond therapy, GNRs also offer distinct advantages for fluorescence imaging due to their unique optical features, such as two-photon luminescence (TPL) and emission in the NIR-II window. Xiao et al. integrated intrinsically cytotoxic NIR dyes with GNRs to enable simultaneous imaging and therapy via TPL-guided activation [88,89]. More recent innovations, such as donor–acceptor–donor (D-A-D) structured boron-dipyrromethene dyes, have pushed emission deeper into the NIR-II range (1000–1700 nm), enabling real-time, high-resolution imaging with enhanced tissue penetration during both photodynamic and photothermal therapy [90]. Gold nanorod vesicles (AuNR Ves) have further advanced theranostics by integrating NIR-II photoacoustic imaging with stimuli-responsive drug release, where complement activation was effectively mitigated through PEGylation [91].

Consistent with previous findings from our team demonstrating that TRAIL's pro-apoptotic potential can be increased in MDA-MB-231 by either mild hyperthermia [30] or photothermal therapy, when conjugated to iron nanoparticles [24] we now demonstrate that gold nanorods conjugated with an agonist anti-DR4 antibody respond effectively to near-infrared (NIR) stimulation, with PTT further enhancing apoptosis in a DR4-specific manner (Fig. 8). Compared to conventional PTT or TRAIL-based therapies, this nanovector offers a dual-function strategy, as it combines tumor-selective targeting and cytotoxicity via anti-DR4 with the remote, heat-inducing properties of GNRs. Importantly, given that this PTT approach inhibits a key negative regulator of the TRAIL pathway, which is thermally suppressed by mild hyperthermia, it enables a reduction of the activation threshold of the TRAIL-mediated pro-apoptotic pathway, resulting in a synergistic enhancement of cell death [24,30].

Recent advances in the field support the value of such synergistic approaches. For example, the photosensitizer NBDPBr has demonstrated a high singlet oxygen quantum yield ( $\Phi = 66\%$ ) and strong photothermal conversion efficiency ( $\eta = 43\%$ ) when encapsulated in amphiphilic F-127 polymer nanoparticles, enabling photoacoustic imaging-guided PTT/PDT in tumor models [92]. While this system shows excellent performance, it lacks the ability to trigger receptor-mediated apoptotic pathways, as provided by our DR4-targeted strategy. Similarly, B-2TPA, a donor–acceptor–donor structured dye, was developed to overcome limitations in NIR absorption and photothermal efficiency. When encapsulated in nanoparticles, B-2TPA demonstrated enhanced singlet oxygen generation ( $\Phi = 6.7\%$ ) and high photothermal conversion efficiency ( $\eta = 60.1\%$ ), validated in both *in vitro* and *in vivo* models [90].

Our approach aligns with these emerging technologies while offering an added layer of therapeutic specificity. By incorporating DR4-specific antibody conjugation, we introduce targeted photothermal sensitization along with receptor-mediated apoptosis induction, a dual mechanism not typically available in current NIR-responsive agents. This strategy holds promise for improving tumor selectivity and minimizing systemic toxicity.

Although we have not yet been able to assess *in vivo* toxicity and biocompatibility due to the limited stability, low synthetic yield, and a pronounced tendency of the GNRs to adhere to container surfaces (including plastic and glass), we remain optimistic about their potential.

Gold nanorods are widely regarded as promising nanomaterials for biomedical applications, including photothermal therapy (PTT), due to their relatively low inherent toxicity compared to other inorganic nanomaterials [11–13,88,93–100].

Toxicity profiles of GNRs hinge on surface chemistry rather than aspect ratio. Cetyltrimethylammonium bromide (CTAB)-coated GNRs induce apoptosis through mitochondrial ROS generation, but this toxicity can be abolished by replacing CTAB with biocompatible polymers such as PSS or PAH [101–103]. DBCO click chemistry minimized complement activation compared to thiol-maleimide conjugation, reducing hematocrit fluctuations and platelet depletion *in vivo* [85]. Long-term studies (15 months) confirmed the safety of PEGylated or rifampicin-conjugated GNRs, with no residual toxicity observed in murine models [102]. Bioorthogonal strategies, such as pretargeting with tetrazine-modified GNRs, further enhanced specificity and reduced off-target effects in stem cell homing applications [104]. These advancements underscore the importance of rational surface engineering to balance therapeutic efficacy with biosafety, paving the way for clinical translation of GNR-based theranostics.

Although current limitations such as low synthetic yield and surface adhesion of GNRs, prevented full evaluation of the DR4 agonist antibody DBCO-grafted onto gold nanorods for NIR-induced photothermal efficiency and receptor-mediated apoptosis *in vivo*, the biocompatibility of GNRs is well-established when appropriate surface modifications are applied. CTAB, a toxic synthesis surfactant, can be replaced with PSS, PAH, or PEG to mitigate cytotoxicity the critical need to remove cetyltrimethylammonium bromide (CTAB), a highly toxic surfactant used during GNR synthesis [105,106]. For full biocompatibility, future studies should explore surface modification of PARA-functionalized GNRs such as PEGylation or hydrophilic sulfoxide-containing polymers [97,107], in order to improve colloidal stability and assess their biodistribution and safety profile *in vivo*.

## 5. Conclusion

This study provides the first demonstration that site-specific functionalization of a pro-apoptotic DR4 agonistic antibody onto DBCO-grafted gold nanorods (GNRs) via click chemistry, enhances both NIR-induced photothermal efficiency and receptor-mediated apoptosis. Unlike conventional conjugation methods (e.g., EDC/NHS or Schiff base), our SPAAC strategy preserves antibody bioactivity and promotes therapeutic selectivity.

Our dual-action platform, which integrates receptor targeting and activation with remote photothermal therapy (PTT), outperforms existing TRAIL- or dye-based systems efficacy. This technology also opens new possibilities for real-time image-guided therapy due to the optical properties of GNRs and their compatibility with contrast agents like Wazabi [90,92].

Future work will focus on surface engineering to improve stability and yield, and *in vivo* validation, but these findings already mark a substantial step toward clinically translatable, highly selective cancer nanotherapies.

## Author contributions

A.R. performed all experiments shown in Figs. 3–8 and was supervised by O.M. M.R. synthesized GNRs and performed experiments shown in Figs. 1–2 and Table 1 and was supervised by N.M.. E.C. synthesized Wazabi and was supervised by C.G.. N.M., G.H. and F.P. generated the Laser which was used in some experiments and helped O.M. and A.R. master its application to obtain the rise of temperature expected. O.M. prepared all figures. A.R., M.R., N.M. and O.M. designed the study, analyzed the data and wrote the main manuscript text, which was reviewed and corrected by all authors.

## Declaration of Generative AI and AI-assisted technologies in the writing process

During the preparation of this work the author(s) used CHATGPT in order to increase concision and clarity of the Abstract, Statement of significance, Introduction, Discussion, and Conclusion. After using this tool/service, the author(s) reviewed and edited the content as needed and take(s) full responsibility for the content of the publication.

## CRedit authorship contribution statement

**Abdelmnim Radoua:** Writing – review & editing, Writing – original draft, Methodology, Investigation, Formal analysis, Data curation, Conceptualization. **Mélanie Romain:** Writing – review & editing, Writing – original draft, Validation, Methodology, Investigation, Formal analysis, Data curation, Conceptualization. **Elisa Chazeau:** Methodology, Investigation, Data curation, Conceptualization. **Nadège Marthouret:** Methodology, Investigation, Conceptualization. **Fabien Picaud:** Writing – review & editing, Formal analysis, Data curation, Conceptualization. **Guillaume Herlem:** Writing – review & editing, Formal analysis, Data curation, Conceptualization. **Christine Goze:** Writing – review & editing, Formal analysis, Data curation, Conceptualization. **Nadine Millot:** Writing – review & editing, Methodology, Funding acquisition, Formal analysis, Data curation, Conceptualization. **Olivier Micheau:** Writing – review & editing, Writing – original draft, Visualization, Validation, Supervision, Resources, Project administration, Methodology, Funding acquisition, Formal analysis, Data curation, Conceptualization.

## Funding

O.M. is supported by grants from the ANR (Agence Nationale de la Recherche) program “Investissements d’Avenir” Labex LipSTIC (ANR-11-LABX-0021-01), ANR ISITE-BFC (ANR-15-IDEX-0003), and ANR LabCom IAM-IT (ANR-22-LCV1-0005-01), the Conseil Régional de Bourgogne (Theracat), the European commission’s Horizon 2020 Research and Innovation Program DISCOVER (777995) and CHIRON (101130240). The DesCarTes team is supported by the Inserm and the Université de Bourgogne Europe. A.R. was supported by a fellowship from the ANR ISITE-BFC (ANR-15-IDEX-0003) and (ANR-22-LCV1-0005-01). NM and MR benefit from the PIA-excellence ISITE-BFC (COMICS project “Chemistry of Molecular Interactions Catalysis and Sensors” FEDER). M.R. thanks the “Conseil Régional de Bourgogne Franche-Comté” and the EIPHI Graduate School (contract ANR-17-EURE-0002) for financial support of her PhD project. Views and opinions expressed are those of the author(s) only and do not necessarily reflect those of the European Union or European Innovation Council and SMEs Executive Agency (EISMEA). Neither the European Union nor the granting authority can be held responsible for them.

## Declaration of competing interest

The authors declare that they have no known competing financial interests or personal relationships that could have appeared to influence the work reported in this paper.

## Acknowledgements

Monoclonal antibodies targeting DR4 and DR5 used for flow cytometry as well as the hybridoma expressing the anti-DR4 antibody used in this study were kindly provided by Covalab. The authors acknowledge the Cytometry Core Facility from the UMS Biosand for their constant support (Université Bourgogne Europe). The authors acknowledge Dr. R. Chassagnon and Dr. O. Heintz of ARCEM-Carnot platform (ICB, Université Bourgogne Europe) for TEM observations and XPS investigations and Dr. Lucien Saviot for Raman spectroscopy

investigations.

## Appendix A. Supplementary data

Supplementary data to this article can be found online at <https://doi.org/10.1016/j.matdes.2025.114212>.

## Data availability

All data generated or analyzed during this study are included in this published article [and its [Supplementary Information Files](#)].

## References

- [1] R.L. Siegel, K.D. Miller, N.S. Wagle, A. Jemal, Cancer statistics, 2023, CA: A Cancer J. Clin. 73 (1) (2023) 17–48.
- [2] K.F. Chu, D.E. Dupuy, Thermal ablation of tumours: biological mechanisms and advances in therapy, Nat. Rev. Cancer 14 (3) (2014) 199–208.
- [3] V. Pansare, S. Hejazi, W. Faenza, R.K. Prud’homme, Review of long-wavelength optical and NIR imaging materials: contrast agents, fluorophores and multifunctional nano carriers, Chem. Mater. 24 (5) (2012) 812–827.
- [4] X. Deng, Z. Shao, Y. Zhao, Solutions to the drawbacks of photothermal and photodynamic cancer therapy, Adv. Sci. 8 (3) (2021) 2002504.
- [5] J. Chen, Z. Ye, F. Yang, Y. Yin, Plasmonic nanostructures for photothermal conversion, Small Sci. 1 (2) (2021) 2000055.
- [6] X. Cui, Q. Ruan, X. Zhuo, X. Xia, J. Hu, R. Fu, Y. Li, J. Wang, H. Xu, Photothermal nanomaterials: a powerful light-to-heat converter, Chem. Rev. 123 (11) (2023) 6891–6952.
- [7] L. Bianchi, R. Mooney, Y.R. Cornejo, E. Schena, J.M. Berlin, K.S. Aboody, P. Saccomandi, Thermal analysis of laser irradiation-gold nanorod combinations at 808 nm, 940 nm, 975 nm and 1064 nm wavelengths in breast cancer model, Int. J. Hyperth. 38 (1) (2021) 1099–1110.
- [8] R. Mooney, E. Schena, P. Saccomandi, A. Zhumkhwala, K. Aboody, J.M. Berlin, Gold nanorod-mediated near-infrared laser ablation: in vivo experiments on mice and theoretical analysis at different settings, Int. J. Hyperth. 33 (2) (2017) 150–159.
- [9] J. Pérez-Juste, I. Pastoriza-Santos, L.M. Liz-Marzán, P. Mulvaney, Gold nanorods: synthesis, characterization and applications, Coord. Chem. Rev. 249 (17) (2005) 1870–1901.
- [10] X. Huang, I.H. El-Sayed, W. Qian, M.A. El-Sayed, Cancer cell imaging and photothermal therapy in the near-infrared region by using gold nanorods, J. Am. Chem. Soc. 128 (6) (2006) 2115–2120.
- [11] H. Huang, Z. Xie, N. Li, L. Zeng, Q. Zeng, Z. Yang, J. Shen, H. Yang, Y. Liu, C. Wu, Biomimetic gold nano-modulator for deep-tumor NIR-II photothermal immunotherapy via gaseous microenvironment remodeling strategy, J. Nanobiotechnol. 23 (1) (2025) 220.
- [12] K. Kim, M.R. Chejara, B. Yoon, M.H. Park, Gold nanorod-based smart platform for efficient cellular uptake and combination therapy, RSC Adv. 14 (37) (2024) 27385–27393.
- [13] H. Liu, C. Gao, P. Xu, Y. Li, X. Yan, X. Guo, C. Wen, X.C. Shen, Biomimetic gold nanorods-manganese porphyrins with surface-enhanced raman scattering effect for photoacoustic imaging-guided photothermal/photodynamic therapy, Small 20 (42) (2024) e2401117.
- [14] A. Dubuisson, O. Micheau, Antibodies and derivatives targeting DR4 and DR5 for cancer therapy, Antibodies (Basel) 6 (2017).
- [15] A. Ashkenazi, R.S. Herbst, To kill a tumor cell: the potential of proapoptotic receptor agonists, J. Clin. Invest. 118 (6) (2008) 1979–1990.
- [16] O. Micheau, Posttranslational modifications and death receptor signalling, in: O. Micheau (Ed.), TRAIL, Fas Ligand, TNF and TLR3 in Cancer, Springer International Publishing, Cham, 2017, pp. 247–290.
- [17] R.M. Pitti, S.A. Marsters, S. Ruppert, C.J. Donahue, A. Moore, A. Ashkenazi, Induction of apoptosis by Apo-2 ligand, a new member of the tumor necrosis factor cytokine family, J. Biol. Chem. 271 (22) (1996) 12687–12690.
- [18] M. Sica, M. Roussel, P. Legembre, CD95/Fas stoichiometry in future precision medicine, Cell Death Differ. (2025).
- [19] H. Walczak, R.E. Miller, K. Ariail, B. Gliniak, T.S. Griffith, M. Kubin, W. Chin, J. Jones, A. Woodward, T. Le, C. Smith, P. Smolak, R.G. Goodwin, C.T. Rauch, J. C. Schuh, D.H. Lynch, Tumoricidal activity of tumor necrosis factor-related apoptosis-inducing ligand in vivo, Nat. Med. 5 (2) (1999) 157–163.
- [20] G.V. Georgakis, Y. Li, R. Humphreys, M. Andreeff, S. O’Brien, M. Younes, A. Carbone, V. Albert, A. Younes, Activity of selective fully human agonistic antibodies to the TRAIL death receptors TRAIL-R1 and TRAIL-R2 in primary and cultured lymphoma cells: induction of apoptosis and enhancement of doxorubicin- and bortezomib-induced cell death, Br. J. Haematol. 130 (4) (2005) 501–510.
- [21] M.J. Smyth, K. Takeda, Y. Hayakawa, J.J. Peschon, M.R. van den Brink, H. Yagita, Nature’s TRAIL-on a path to cancer immunotherapy, Immunity 18 (1) (2003) 1–6.
- [22] D. de Miguel, J. Lemke, A. Anel, H. Walczak, L. Martinez-Lostao, Onto better TRAILs for cancer treatment, Cell Death Differ. 23 (5) (2016) 733–747.
- [23] H. Belkahl, G. Herlem, F. Picaud, T. Gharbi, M. Hemadi, S. Ammar, O. Micheau, TRAIL-NP hybrids for cancer therapy: a review, Nanoscale 9 (18) (2017) 5755–5768.

- [24] H. Belkahlia, E. Mazario, A.P. Sangnier, J.S. Lomas, T. Gharbi, S. Ammar, O. Micheau, C. Wilhelm, M. Hemadi, TRAIL acts synergistically with iron oxide nanocluster-mediated magneto- and photothermia, *Theranostics* 9 (20) (2019) 5924–5936.
- [25] A.B. Zakaria, F. Picaud, T. Rattier, M. Pudlo, F. Dufour, L. Saviot, R. Chassagnon, J. Lherminier, T. Gharbi, O. Micheau, G. Herlem, Nanovectorization of TRAIL with single wall carbon nanotubes enhances tumor cell killing, *Nano Lett.* 15 (2) (2015) 891–895.
- [26] Y. Kim, J. Kim, S. Eom, H. Jun, H.B. Lee, D. Jeong, S. Kang, Protein nanoparticles simultaneously displaying TRAIL and EGFR-binding ligands effectively induce apoptotic cancer cell death and overcome EGFR-TKI resistance in lung cancer, *ACS Appl. Mater. Interfaces* (2025).
- [27] S. Liu, Z. Ji, S. Ge, C. Cai, H. Zhang, Y. Wang, Y. Zhou, J. Zhou, H. Cheng, Y. Ding, Cascade-targeting apoptosis via synergy of TRAIL-specific bystander effect and mitochondrial photodamage in cancer therapy, *Nano Lett.* 25 (14) (2025) 5881–5890.
- [28] T.T.K. Nguyen, S.M. Woo, S.U. Seo, A. Banstola, H. Kim, R. Duwa, A.T.T. Vu, I. S. Hong, T.K. Kwon, S. Yook, Enhanced anticancer efficacy of TRAIL-conjugated and odanacatib-loaded PLGA nanoparticles in TRAIL resistant cancer, *Biomaterials* 312 (2025) 122733.
- [29] A.A. Farooqi, A. Turgambayeva, G. Kamalbekova, R. Suleimenova, N. Latypova, S. Ospanova, D. Ospanova, Z. Abdikadyr, S. Zhussupov, TRAIL as a warrior in nano-sized trojan horse: anticancer and anti-metastatic effects of nano-formulations of TRAIL in cell culture and animal model studies, *Medicina (Kaunas)* 60 (12) (2024).
- [30] A. Morle, C. Garrido, O. Micheau, Hyperthermia restores apoptosis induced by death receptors through aggregation-induced c-FLIP cytosolic depletion, *Cell Death Dis.* 6 (2015) e1633.
- [31] H. Belkahlia, A.A. Constantinescu, T. Gharbi, F. Barbault, A. Chevillot-Biraud, P. Decorse, O. Micheau, M. Hemadi, S. Ammar, Grafting TRAIL through either amino or carboxylic groups onto maghemite nanoparticles: influence on pro-apoptotic efficiency, *Nanomaterials (Basel)* 11 (2) (2021).
- [32] M. Arruebo, M. Valladares, Á. González-Fernández, Antibody-conjugated nanoparticles for biomedical applications, *J. Nanomater.* 2009 (2009) 439389.
- [33] J.-M. Montenegro, V. Grazu, A. Sukhanova, S. Agarwal, J.M. de la Fuente, I. Nabiev, A. Greiner, W.J. Parak, Controlled antibody/(bio-) conjugation of inorganic nanoparticles for targeted delivery, *Adv. Drug Deliv. Rev.* 65 (5) (2013) 677–688.
- [34] K. Upadhyay, R.K. Tamrakar, S. Thomas, M. Kumar, Surface functionalized nanoparticles: a boon to biomedical science, *Chem. Biol. Interact.* 380 (2023) 110537.
- [35] L. Nobs, F. Buchegger, R. Gurny, E. Allémann, Current methods for attaching targeting ligands to liposomes and nanoparticles, *J. Pharm. Sci.* 93 (8) (2004) 1980–1992.
- [36] A.C. Marques, P.J. Costa, S. Velho, M.H. Amaral, Functionalizing nanoparticles with cancer-targeting antibodies: a comparison of strategies, *J. Control. Release* 320 (2020) 180–200.
- [37] E. Steen Redeker, D.T. Ta, D. Cortens, B. Billen, W. Guedens, P. Adriaensens, Protein engineering for directed immobilization, *Bioconjug. Chem.* 24 (11) (2013) 1761–1777.
- [38] J. Conde, J.T. Dias, V. Grazú, M. Moros, P.V. Baptista, J.M. de la Fuente, Revisiting 30 years of biofunctionalization and surface chemistry of inorganic nanoparticles for nanomedicine, *Front. Chem.* 2 (2014).
- [39] C.-T. Jiang, K.-G. Chen, A. Liu, H. Huang, Y.-N. Fan, D.-K. Zhao, Q.-N. Ye, H.-B. Zhang, C.-F. Xu, S. Shen, M.-H. Xiong, J.-Z. Du, X.-Z. Yang, J. Wang, Immunomodulating nano-adaptors potentiate antibody-based cancer immunotherapy, *Nat. Commun.* 12 (1) (2021) 1359.
- [40] C.D. Hein, X.-M. Liu, D. Wang, Click chemistry, A powerful tool for pharmaceutical sciences, *Pharm. Res.* 25 (10) (2008) 2216–2230.
- [41] G. Yi, J. Son, J. Yoo, C. Park, H. Koo, Application of click chemistry in nanoparticle modification and its targeted delivery, *Biomater. Res.* 22 (1) (2018) 13.
- [42] E. Kim, H. Koo, Biomedical applications of copper-free click chemistry: in vitro, in vivo, and ex vivo, *Chem. Sci.* 10 (34) (2019) 7835–7851.
- [43] H.C. Kolb, M.G. Finn, K.B. Sharpless, Click chemistry: diverse chemical function from a few good reactions, *Angew. Chem. Int. Ed. Engl.* 40 (11) (2001) 2004–2021.
- [44] F. Dufour, T. Rattier, A.A. Constantinescu, L. Zischler, A. Morle, H. Ben Mabrouk, E. Humblin, G. Jacquemin, E. Szegezdi, F. Delacote, N. Marrakchi, G. Guichard, C. Pellat-Deceunynck, P. Vacher, P. Legembre, C. Garrido, O. Micheau, TRAIL receptor gene editing unveils TRAIL-R1 as a master player of apoptosis induced by TRAIL and ER stress, *Oncotarget* 8 (6) (2017) 9974–9985.
- [45] A. Dubuisson, C. Favreau, E. Fourmaux, S. Lareure, R. Rodrigues-Saraiva, C. Pellat-Deceunynck, S. El Alaoui, O. Micheau, Generation and characterization of novel anti-DR4 and anti-DR5 antibodies developed by genetic immunization, *Cell Death Dis.* 10 (2) (2019) 101.
- [46] S. von Karstedt, A. Conti, M. Nobis, A. Montinaro, T. Hartwig, J. Lemke, K. Legler, F. Annenwarter, A.D. Campbell, L. Taraborrelli, A. Grosse-Wilde, J.F. Coy, M.A. El-Bahrawy, F. Bergmann, R. Koschny, J. Werner, T.M. Ganten, T. Schweiger, K. Hoetzenecker, I. Kenessey, B. Hegedus, M. Bergmann, C. Hauser, J.H. Egberts, T. Becker, C. Rocken, H. Kalthoff, A. Trauzold, K.I. Anderson, O.J. Sansom, H. Walczak, Cancer cell-autonomous TRAIL-R signaling promotes KRAS-driven cancer progression, invasion, and metastasis, *Cancer Cell* 27 (4) (2015) 561–573.
- [47] K.A. Kozek, K.M. Kozek, W.-C. Wu, S.R. Mishra, J.B. Tracy, Large-scale synthesis of gold nanorods through continuous secondary growth, *Chem. Mater.* 25 (22) (2013) 4537–4544.
- [48] L. Scarabelli, A. Sánchez-Iglesias, J. Pérez-Juste, L.M. Liz-Marzán, A “tips and tricks” practical guide to the synthesis of gold nanorods, *J. Phys. Chem. Lett.* 6 (21) (2015) 4270–4279.
- [49] H. Zhu, J. Yan, Q. Xu, L. Wei, X. Huang, S. Chen, C. Yi, TRAIL mutant membrane penetrating peptide alike (TMPPA) TRAIL-Mu3 enhances the antitumor effects of TRAIL in vitro and in vivo, *Mol. Med. Rep.* 16 (6) (2017) 9607–9612.
- [50] A. Radoua, B. Pernon, N. Pernet, C. Jean, M. Elmallah, A. Guerrache, A. A. Constantinescu, S. Hadj Hamou, J. Devy, O. Micheau, pARgenOM-a flexible vector for CRISPR/CAS9 nonviral delivery, *Small Methods* 7 (7) (2023) e2300069.
- [51] M.M. Miller, A.A. Lazarides, Sensitivity of metal nanoparticle surface plasmon resonance to the dielectric environment, *J. Phys. Chem. B* 109 (46) (2005) 21556–21565.
- [52] Z. Zhang, M. Lin, Fast loading of PEG-SH on CTAB-protected gold nanorods, *RSC Adv.* 4 (34) (2014) 17760–17767.
- [53] R. Stiuftuc, B. Iacovita, R. Nicoara, G. Stiuftuc, A. Florea, M. Achim, C.M. Lucaciu, One-step synthesis of PEGylated gold nanoparticles with tunable surface charge, *J. Nanomater.* 2013 (2013) 146031.
- [54] V.V. Kuzmin, V.S. Novikov, L.Y. Ustyinyuk, K.A. Prokhorov, E.A. Sagitova, G. Y. Nikolaeva, Raman spectra of polyethylene glycols: comparative experimental and DFT study, *J. Mol. Struct.* 1217 (2020) 128331.
- [55] S.P. Somasekharan, M. Koc, A. Morizot, O. Micheau, P.H. Sorensen, O. Gaide, L. Andera, J.C. Martinou, TRAIL promotes membrane blebbing, detachment and migration of cells displaying a dysfunctional intrinsic pathway of apoptosis, *Apoptosis* 18 (3) (2013) 324–336.
- [56] H. Wang, J.S. Davis, X. Wu, Immunoglobulin fc domain fusion to TRAIL significantly prolongs its plasma half-life and enhances its antitumor activity, *Mol. Cancer Ther.* 13 (3) (2014) 643–650.
- [57] A. Algeciras-Schimnich, L. Shen, B.C. Barnhart, A.E. Murmann, J.K. Burkhardt, M. E. Peter, Molecular ordering of the initial signaling events of CD95, *Mol. Cell Biol.* 22 (1) (2002) 207–220.
- [58] O. Micheau, Regulation of TNF-related apoptosis-inducing ligand signaling by glycosylation, *Int. J. Mol. Sci.* 19 (3) (2018).
- [59] Y. Ge, D.F. O’Shea, Azadipyrromethenes: from traditional dye chemistry to leading edge applications, *Chem. Soc. Rev.* 45 (14) (2016) 3846–3864.
- [60] Z. Shi, X. Han, W. Hu, H. Bai, B. Peng, L. Ji, Q. Fan, L. Li, W. Huang, Bioapplications of small molecule aza-BODIPY: from rational structural design to in vivo investigations, *Chem. Soc. Rev.* 49 (21) (2020) 7533–7567.
- [61] A. Kamkaew, K. Burgess, Aza-BODIPY dyes with enhanced hydrophilicity, *Chem. Commun.* 51 (53) (2015) 10664–10667.
- [62] J. Pliquett, A. Dubois, C. Racour, N. Mabrouk, S. Amor, R. Lescure, A. Betteieb, B. Collin, C. Bernhard, F. Denat, P.S. Bellaye, C. Paul, E. Bodio, C. Goze, A promising family of fluorescent water-soluble aza-BODIPY dyes for in vivo molecular imaging, *Bioconjug. Chem.* 30 (4) (2019) 1061–1066.
- [63] F. Di Cristofano, A. George, V. Tajiknia, M. Ghandali, L. Wu, Y. Zhang, P. Srinivasan, J. Strandberg, M. Hahn, A. Sanchez Sevilla Urchurtu, A.A. Seyhan, B.A. Carneiro, L. Zhou, K.E. Huntington, W.S. El-Deiry, Therapeutic targeting of TRAIL death receptors, *Biochem. Soc. Trans.* 51 (1) (2023) 57–70.
- [64] A. Montinaro, H. Walczak, Harnessing TRAIL-induced cell death for cancer therapy: a long walk with thrilling discoveries, *Cell Death Differ.* 30 (2) (2023) 237–249.
- [65] M. Snajdauf, K. Havlova, J. Vachtenheim Jr., A. Ozaniak, R. Lischke, J. Bartunkova, D. Smrz, Z. Strizova, The TRAIL in the treatment of human cancer: an update on clinical trials, *Front. Mol. Biosci.* 8 (2021) 628332.
- [66] O. Micheau, S. Shirley, F. Dufour, Death receptors as targets in cancer, *Br. J. Pharmacol.* 169 (8) (2013) 1723–1744.
- [67] X. Ouyang, M. Shi, F. Jie, Y. Bai, P. Shen, Z. Yu, X. Wang, C. Huang, M. Tao, Z. Wang, C. Xie, Q. Wu, Y. Shu, B. Han, F. Zhang, Y. Zhang, C. Hu, X. Ma, Y. Liang, A. Wang, B. Lu, Y. Shi, J. Chen, Z. Zhuang, J. Wang, J. Huang, C. Wang, C. Bai, X. Zhou, Q. Li, F. Chen, H. Yu, J. Feng, Phase III study of dulaneerin (recombinant human tumor necrosis factor-related apoptosis-inducing ligand/Apo2 ligand) combined with vinorelbine and cisplatin in patients with advanced non-small-cell lung cancer, *Invest. New Drugs* 36 (2) (2018) 315–322.
- [68] O. Micheau, M. Rizzi, C.R. Smulski, Editorial: TNFR superfamily oligomerization and signaling, *Front. Cell Dev. Biol.* 9 (2021) 682472.
- [69] P. LoRusso, M.J. Ratain, T. Doi, D.W. Rasco, M.J.A. de Jonge, V. Moreno, B. A. Carneiro, L.A. Devriese, A. Petrich, D. Modi, S. Morgan-Lappe, S. Nuthalapati, M. Motwani, M. Dunbar, J. Glasgow, B.C. Medeiros, E. Calvo, Eftozanermin alfa (ABBV-621) monotherapy in patients with previously treated solid tumors: findings of a phase 1, first-in-human study, *Invest. New Drugs* 40 (4) (2022) 762–772.
- [70] N. Ma, K. Cheng, Q. Feng, G. Liu, J. Liang, X. Ma, Z. Chen, Y. Lu, X. Wang, W. He, H. Xu, S. Wu, J. Zou, Q. Shi, G. Nie, X. Zhao, Nanoscale organization of TRAIL trimers using DNA origami to promote clustering of death receptor and cancer cell apoptosis, *Small* 19 (23) (2023) e2206160.
- [71] T. Tamada, D. Shinmi, M. Ikeda, Y. Yonezawa, S. Kataoka, R. Kuroki, E. Mori, K. Motoki, TRAIL-R2 superoligomerization induced by human monoclonal agonistic antibody KMTR2, *Sci. Rep.* 5 (2015) 17936.
- [72] V. Pavet, J. Beyrath, C. Pardin, A. Morizot, M.-C. Lechner, J.-P. Briand, M. Wendland, W. Maisson, S. Fournel, O. Micheau, G. Guichard, H. Gronemeyer, Multivalent DR5 peptides activate the TRAIL death pathway and exert tumoricidal activity, *Cancer Res.* 70 (2010) 1101–1110.
- [73] X. Piao, T. Ozawa, H. Hamana, K. Shitaoka, A. Jin, H. Kishi, A. Muraguchi, TRAIL-receptor 1 IgM antibodies strongly induce apoptosis in human cancer cells in vitro and in vivo, *Oncoimmunology* 5 (5) (2016) e1131380.

- [74] D. De Miguel, A. Gallego-Lleyda, A. Anel, L. Martinez-Lostao, Liposome-bound TRAIL induces superior DR5 clustering and enhanced DISC recruitment in histiocytic lymphoma U937 cells, *Leuk. Res.* 39 (6) (2015) 657–666.
- [75] O. Seifert, N. Pollak, A. Nusser, F. Steiniger, R. Ruger, K. Pfitzenmaier, R. E. Kontermann, Immuno-LipoTRAIL: targeted delivery of TRAIL-functionalized liposomal nanoparticles, *Bioconjug. Chem.* 25 (5) (2014) 879–887.
- [76] F. Liu, Y. Si, G. Liu, S. Li, J. Zhang, Y. Ma, The tetravalent anti-DR5 antibody without cross-linking direct induces apoptosis of cancer cells, *Biomed. Pharmacother.* 70 (2015) 41–45.
- [77] P.T. Sujai, M.M. Joseph, V. Karunakaran, G. Saranya, R.N. Adukkadan, S. Shamjith, R. Thomas, J.B. Nair, R.S. Swathi, K.K. Maiti, Biogenic cluster-encased gold nanorods as a targeted three-in-one theranostic nanoenvelope for SERS-guided photochemotherapy against metastatic melanoma, *ACS Appl. Bio Mater.* 2 (1) (2019) 588–600.
- [78] S. Tummala, M.N. Kumar, S.K. Pindiprolu, Improved anti-tumor activity of oxaliplatin by encapsulating in anti-DR5 targeted gold nanoparticles, *Drug Deliv.* 23 (9) (2016) 3505–3519.
- [79] M. Krishnamoorthy, S. Hakobyan, M. Ramstedt, J.E. Gautrot, Surface-initiated polymer brushes in the biomedical field: applications in membrane science, biosensing, cell culture, regenerative medicine and antibacterial coatings, *Chem. Rev.* 114 (21) (2014) 10976–11026.
- [80] M. Li, S. Jiang, J. Simon, D. Passlick, M.L. Frey, M. Wagner, V. Mailander, D. Crespy, K. Landfester, Brush conformation of polyethylene glycol determines the stealth effect of nanocarriers in the low protein adsorption regime, *Nano Lett.* 21 (4) (2021) 1591–1598.
- [81] G. Fibriansah, J.L. Tan, S.A. Smith, R. de Alwis, T.S. Ng, V.A. Kostyuchenko, R. S. Jadi, P. Kukkaro, A.M. de Silva, J.E. Crowe, S.M. Lok, A highly potent human antibody neutralizes dengue virus serotype 3 by binding across three surface proteins, *Nat. Commun.* 6 (2015) 6341.
- [82] A. Azulay, L. Cohen-Lavi, L.M. Friedman, M.A. McGargill, T. Hertz, Mapping antibody footprints using binding profiles, *Cell Rep. Methods* 3 (8) (2023) 100566.
- [83] A.K. Trilling, J. Beekwilder, H. Zuilhof, Antibody orientation on biosensor surfaces: a minireview, *Analyst* 138 (6) (2013) 1619–1627.
- [84] E. Maksimova, D.E. Salazar Marcano, J. De Roo, Quantification of azides on the surface of nanoparticles: toward precise bioconjugation, *Small Struct.* n/a(n/a) 2500083.
- [85] M.H. Zaleski, L.S. Chase, E.D. Hood, Z. Wang, J. Nong, C.L. Espy, M.E. Zamora, J. Wu, L.J. Morrell, V.R. Muzykantov, J.W. Myerson, J.S. Brenner, Conjugation chemistry Markedly impacts toxicity and biodistribution of targeted nanoparticles, mediated by complement activation, *Adv. Mater.* 37 (5) (2025) e2409945.
- [86] B. Feng, Z. Xu, F. Zhou, H. Yu, Q. Sun, D. Wang, Z. Tang, H. Yu, Q. Yin, Z. Zhang, Y. Li, Near infrared light-actuated gold nanorods with cisplatin-polypeptide wrapping for targeted therapy of triple negative breast cancer, *Nanoscale* 7 (36) (2015) 14854–14864.
- [87] F. Oudjedi, A.G. Kirk, Near-infrared nanoparticle-mediated photothermal cancer therapy: a comprehensive review of advances in monitoring and controlling thermal effects for effective cancer treatment, *Nano Select* 6 (3) (2025) e202400107.
- [88] Y.F. Xiao, F.F. An, J.X. Chen, J. Yu, W.W. Tao, Z. Yu, R. Ting, C.S. Lee, X. H. Zhang, The nanoassembly of an intrinsically cytotoxic near-infrared dye for multifunctionally synergistic theranostics, *Small* 15 (38) (2019) e1903121.
- [89] L. Tong, Q. Wei, A. Wei, J.-X. Cheng, Gold nanorods as contrast agents for biological imaging: optical properties, surface conjugation and photothermal effects, *Photochem. Photobiol.* 85 (1) (2009) 21–32.
- [90] X. Xing, P. Zhu, E. Pang, S. Zhao, Y. Tang, Z. Hu, Q. Ouyang, M. Lan, D-A-D-structured boron-dipyrromethene with aggregation-induced enhanced phototherapeutic efficiency for near-infrared fluorescent and photoacoustic imaging-guided synergistic photodynamic and photothermal cancer therapy, *Chin. Chem. Lett.* 35 (10) (2024) 109452.
- [91] X. Ge, Q. Fu, L. Su, Z. Li, W. Zhang, T. Chen, H. Yang, J. Song, Light-activated gold nanorod vesicles with NIR-II fluorescence and photoacoustic imaging performances for cancer theranostics, *Theranostics* 10 (11) (2020) 4809–4821.
- [92] L. Wang, A. Mei, N. Li, X. Ruan, X. Sun, Y. Cai, J. Shao, X. Dong, Aza-BODIPY dye with unexpected bromination and high singlet oxygen quantum yield for photoacoustic imaging-guided synergistic photodynamic/photothermal therapy, *Chin. Chem. Lett.* 35 (6) (2024) 108974.
- [93] M. Debnath, S.K. Debnath, M.V. Talpade, S. Bhatt, P.P. Gupta, R. Srivastava, Surface engineered nanohybrids in plasmonic photothermal therapy for cancer: regulatory and translational challenges, *Nanotheranostics* 8 (2) (2024) 202–218.
- [94] J. Gu, L. Jiang, Z. Chen, J. Qi, A simple nanoplatform of thermo-sensitive liposomes and gold nanorods to treat bone metastasis through improved chemotherapy combined with photothermal therapy, *Int J Pharm X* 8 (2024) 100282.
- [95] B.E. Kennedy, E.B. Nofall, C. Dean, A. Roth, K.N. Clark, D. Rowles, K. Singh, L. Pagliaro, C.A. Giacomantonio, Targeted intra-tumoral hyperthermia using uniquely biocompatible gold nanorods induces strong immunogenic cell death in two immunogenically ‘cold’ tumor models, *Front. Immunol.* 15 (2024) 1512543.
- [96] N. Mustakim, L.F.R. Vera, J.P. Pinto, S.W. Seo, Gold nanorod-embedded PDMS micro-pillar array for localized photothermal stimulation, *J. Microelectromech. Syst.* 33 (5) (2024) 543–549.
- [97] X. Tang, Y. Liu, M. Zhao, L. He, J. Guo, T. Wang, W. Li, J. Zhao, Gold nanorod-loaded nano-contrast agent with composite shell-core structure for ultrasonic/ photothermal imaging-guided therapy in ischemic muscle disorders, *Int. J. Nanomed.* 19 (2024) 4121–4136.
- [98] A. Khoshnood, N. Farhadian, K. Abnous, M.M. Matin, N. Ziaee, S. Iranpour, Polyethyleneimine/gold nanorods conjugated with carbon quantum dots and hyaluronic acid for chemo-photothermal therapy of breast cancer, *J. Mater. Chem. B* (2025).
- [99] L. Song, J. Li, Ultrasensitive NIR-II surface-enhanced resonance Raman scattering nanopropes with nonlinear photothermal effect for optimized phototheranostics, *Small* 21 (4) (2025) e2407787.
- [100] S. Varma, A.L. Bamb, N. Haldar, V. Gajbhiye, D. Amalnerkar, B.P. Chaudhari, Gold nanorods (GNRs): a golden nano compass to navigate breast cancer by multimodal imaging approaches, *J. Biomed. Mater. Res. B Appl. Biomater.* 113 (2) (2025) e35543.
- [101] J. Wan, J.H. Wang, T. Liu, Z. Xie, X.F. Yu, W. Li, Surface chemistry but not aspect ratio mediates the biological toxicity of gold nanorods in vitro and in vivo, *Sci. Rep.* 5 (2015) 11398.
- [102] M.R. Ali, M.A. Rahman, Y. Wu, T. Han, X. Peng, M.A. Mackey, D. Wang, H.J. Shin, Z.G. Chen, H. Xiao, R. Wu, Y. Tang, D.M. Shin, M.A. El-Sayed, Efficacy, long-term toxicity, and mechanistic studies of gold nanorods photothermal therapy of cancer in xenograft mice, *Proc. Natl. Acad. Sci. USA* 114 (15) (2017) E3110–E3118.
- [103] L. Wu, B. Lin, H. Yang, J. Chen, Z. Mao, W. Wang, C. Gao, Enzyme-responsive multifunctional peptide coating of gold nanorods improves tumor targeting and photothermal therapy efficacy, *Acta Biomater.* 86 (2019) 363–372.
- [104] Z. Li, D. Shen, S. Hu, T. Su, K. Huang, F. Liu, L. Hou, K. Cheng, Pretargeting and bioorthogonal click chemistry-mediated endogenous stem cell homing for heart repair, *ACS Nano* 12 (12) (2018) 12193–12200.
- [105] H.J. Laszewski, B. Palpant, M. Buckle, C. Noguez, Influence of the sequestration effect of CTAB on the biofunctionalization of gold nanorods, *ACS Appl. Bio Mater.* 4 (6) (2021) 4753–4759.
- [106] O. Beltran, M. Luna, M. Gastelum, A. Costa-Santos, A. Cambon, P. Taboada, M. A. Lopez-Mata, A. Topete, J. Juarez, Novel gold nanorods@thiolated pectin on the killing of HeLa cells by photothermal ablation, *Pharmaceutics* 15 (11) (2023).
- [107] Y. Chang, Q. Wang, W. Xu, X. Huang, X. Xu, F.Y. Han, R. Qiao, G.R. Ediriweera, H. Peng, C. Fu, K. Liu, A.K. Whittaker, Low-fouling gold nanorod theranostic agents enabled by a sulfoxide polymer coating, *Biomacromolecules* 23 (9) (2022) 3866–3874.